Hyper-Objective Vortices

Tobias Günther and Holger Theisel

Abstract—Almost all properties of vector fields, including magnitude, direction, λ_2 and vorticity change under arbitrary movements of the observer. This is undesirable since measurements of physical properties should ideally not depend on the way the (virtual) measurement device moves. There are some properties that are invariant under certain types of reference frame transformations: Galilean invariance (invariance under equal-speed translation) and objectivity (invariance under any smooth rotation and translation of the reference frame). In this paper, we introduce even harder conditions than objectivity: we demand invariance under any smooth similarity transformation (rotation, translation and uniform scale) as well as invariance under any smooth affine transformation of the reference frame. We show that these new hyper-objective measures allow the extraction of vortices that change their volume or deform. Further, we present a generic approach that transforms almost any vortex measure into a hyper-objective one. We apply our methods to vortex extraction in 2D and 3D vector fields, and analyze the numerical robustness, extraction time and the minimization residuals for the Galilean invariant, objective, and the two new hyper-objective approaches.

Index Terms—Flow visualization, vortex extraction, objectivity, affine invariance

1 Introduction

The extraction of vortices in time-dependent vector fields plays an important role in many scientific problems, including vehicle design in engineering, the transport of microorganisms across the oceans, as well as wind observations in meteorology to name a few. A multitude of formal vortex definitions were proposed over the years [23], [28], [31], but none emerged as the ultimate solution. One reason is that the result of most vortex measures depends on the movement of the reference frame, which limits their reliability in practice. As an illustrating example, consider the flow of a river that is observed from a helicopter above it. Any movement of the helicopter generally leads to different observations of the flow, see Fig. 1. The invariance of a vortex measure under a certain type of reference frame transformation directly translates to the ability to correctly track vortices that perform this type of transformation. Galilean invariant methods, for instance, are able to track vortices that perform equal-speed translations, so-called Galilean transformations. Objectivity is the invariance under any smooth rotation and translation of the reference frame [46], and hence, vortices are allowed to arbitrarily rotate and translate. The recent and (still ongoing) discussion and debate on the objectivity in fluids, and in particular in vortex detection, has been initiated by Haller [14], [16], [27], [39], leading to several objective vortex characterizations. In this paper, we extend the work of Günther et al. [10] to go beyond objectivity. Using a linear optimization, we locally transform any vector field into a reference frame, in which the vector field appears as steady as possible, i.e., in which the temporal derivative of the transformed field vanishes. Thereby, we allow for more general transformations than only rotations and translations to take the vector field into a local optimal reference frame. This includes *similarity transformations* (translation, rotation and uniform scale–the pilot might change altitude), as well as general *affine transformations*–the pilot may also roll the helicopter, which distorts the view.

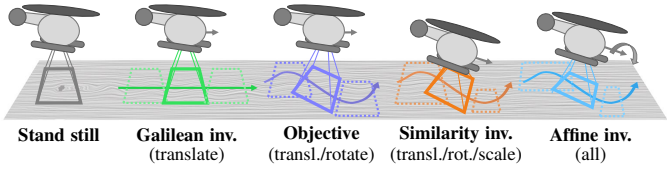

Fig. 1: Overview of reference frame transformations.

We call these methods *hyper-objective* to indicate that they are a generalization of objectivity, which is included as a special case. By restricting the reference frame transformation to the class of Galilean transformations, we show that a subtraction of the feature flow field [43] minimizes the temporal derivative of the resulting field. This proves that the coreline extraction of Weinkauf et al. [47] is optimal when assuming that vortices perform Galilean transformations. The more degrees of freedom the reference frame transformation has, the greater are the numerical difficulties. We study the extraction time, residuals and numerical robustness of all proposed methods in a number of analytic and real-world 2D and 3D vector fields. The contributions of this paper are:

- two novel classes of reference frame invariance, named *similarity invariance* and *affine invariance*,
- a generic framework that makes any property that depends on the velocity or its derivatives *hyper-objective*, i.e., similarity invariant and/or affine invariant,
- a local vector field decomposition that splits a flow into a near-steady reference frame and an ambient transport part,
- a comparison of Galilean invariant [47], objective [10] and hyper-objective vortex coreline extraction methods,
- a proof that subtraction of the feature flow field minimizes the temporal flow derivative for Galilean transformations.

After a brief summary of the notation used in this paper, we provide an overview of related work in the area of vortex extraction in Section 2. The analysis of various types of reference frame transformations follows in Section 3. We start with the most general case (affine invariance) and then gradually decrease the number of degrees of freedom. We introduce similarity invariance, touch upon objectivity [10], and finally arrive at Galilean invariance. A

- *Tobias Günther is with the Computer Graphics Laboratory at ETH Zürich. E-mail: tobias.guenther@inf.ethz.ch*
- *Holger Theisel is head of the Visual Computing Group at University of Magdeburg. E-mail: theisel@ovgu.de*

Manuscript received July 4, 2017; revised xx, 2017.

local optimal vector field decomposition is described in Section 4. Section 5 defines vortex measures in the respective optimal frames. Implementation details are given in Section 6, and all methods are compared and evaluated in Section 7 in a number of 2D and 3D vector fields. The paper closes with a conclusion in Section 8.

Notation

Let $\mathbf{v}(\mathbf{x},t) = \mathbf{v}(x,y[,z],t)$ be an n-dimensional ($n = 2,3$) unsteady vector field, defined in the domain $D \subseteq \mathbb{R}^n$, $\mathbf{x} \in D$:

$$\mathbf{v}(\mathbf{x},t) = \begin{pmatrix} u(\mathbf{x},t) \\ v(\mathbf{x},t) \\ [w(\mathbf{x},t)] \end{pmatrix} \tag{1}$$

Its spatial derivatives are contained in the Jacobian matrix $\mathbf{J} = (\frac{\partial \mathbf{v}}{\partial x}, \frac{\partial \mathbf{v}}{\partial y}[, \frac{\partial \mathbf{v}}{\partial z}])$. We denote the temporal derivative as $\mathbf{v}_t = \frac{\partial \mathbf{v}}{\partial t}$ and thus acceleration becomes $\mathbf{a} = \mathbf{J}\mathbf{v} + \mathbf{v}_t$. The Jacobian $\mathbf{J}$ can be decomposed into the strain rate tensor $\mathbf{S}$ and the vorticity tensor $\mathbf{\Omega}$ as $\mathbf{J} = \mathbf{S} + \mathbf{\Omega}$, with:

$$\mathbf{S} = \frac{\mathbf{J} + \mathbf{J}^{\mathrm{T}}}{2} \qquad \mathbf{\Omega} = \frac{\mathbf{J} - \mathbf{J}^{\mathrm{T}}}{2} \tag{2}$$

where $\mathbf{S}$ is a symmetric and $\mathbf{\Omega}$ is an anti-symmetric matrix. Following [10], we use the function ap that transforms the anti-symmetric part of a matrix to a scalar/vector. In 2D, $ap(\mathbf{M}) = \frac{1}{2}(m_{1,2} - m_{2,1})$. In 3D, $ap(\mathbf{M}) = \frac{1}{2}(m_{3,2} - m_{2,3}\,,\, m_{1,3} - m_{3,1}\,,\, m_{2,1} - m_{1,2})^{\mathrm{T}}$ where $m_{i,j}$ refer to the elements of the matrix $\mathbf{M}$. The inverse of ap is the function sk that transforms a scalar/vector into an antisymmetric matrix. In 2D and 3D, we have:

$$sk(\alpha) = \begin{pmatrix} 0 & \alpha \\ -\alpha & 0 \end{pmatrix} \quad , \quad sk\begin{pmatrix} \alpha \\ \beta \\ \gamma \end{pmatrix} = \begin{pmatrix} 0 & -\gamma & \beta \\ \gamma & 0 & -\alpha \\ -\beta & \alpha & 0 \end{pmatrix} \tag{3}$$

With this, vorticity is defined in 2D and 3D as:

$$\text{2D: } \omega = ap(\mathbf{\Omega}) \qquad \text{3D: } \boldsymbol{\omega} = ap(\mathbf{\Omega}) \tag{4}$$

The operator $vec(\mathbf{M})$ reshapes a matrix into a vector by appending the columns. Further, we denote the Parallel Vectors Operator [28] of two 3D vectors as $\|$, which returns all locations at which two given vector fields are parallel.

Further, we make use of the feature flow field $\mathbf{f}$ [43], [47], which can be defined in space as, cf. [9]:

$$\mathbf{f} = -\mathbf{J}^{-1}\,\mathbf{v}_t\,. \tag{5}$$

The feature flow field gives the direction, in which neither of the vector field components will change over time. It is therefore useful to track features, such as critical points [43].

Later, we denote the identity matrix as $\mathbf{I}$, the trace of matrix $\mathbf{M}$ as $tr(\mathbf{M})$ and the Euclidean norm as $\|\mathbf{M}\| = \sqrt{tr(\mathbf{M}\,\mathbf{M}^{\mathrm{T}})}$.

2 Related Work

In this section, we explain the most commonly used vortex measures. Numerous other vortex extraction methods have been proposed in the literature, and we cannot cover them all. We refer to [13], [23], [28], [31] for a comprehensive overview.

2.1 Region-based Methods

We begin with region-based methods, which calculate a scalar value for each location in the domain. Using these methods, vortex regions are found by suitable thresholding. Next, we classify existing methods into Galilean invariant and objective techniques.

2.1.1 Galilean Invariant Methods

Galilean invariance is the invariance of a measure under equal-speed translations of the reference frame of the form:

$$\mathbf{x}^* = \mathbf{x} + \mathbf{c}_0 + t\,\mathbf{c}_1 \quad , \quad t^* = t - a \tag{6}$$

where $\mathbf{c}_0, \mathbf{c}_1$ are constant vectors. Measures derived from the Jacobian $\mathbf{J}$, acceleration $\mathbf{a}$ and the expression $\mathbf{v} - \mathbf{f}$ are Galilean invariant. Many region-based vortex extraction methods are based on the decomposition of Jacobian $\mathbf{J}$ into its symmetric part $\mathbf{S}$ and its anti-symmetric part $\mathbf{\Omega}$, cf. Eq. (2). In 2D, the signed vorticity ω can be read from the vorticity tensor $\mathbf{\Omega}$. In 3D, vorticity $\boldsymbol{\omega}$ is vector-valued, and its magnitude $|\boldsymbol{\omega}|$ relates to rotational speed, see Eq. (4). Jeong and Hussain [18] characterized vortices as regions in which the second-largest eigenvalue of $\mathbf{S}^2 + \mathbf{\Omega}^2$ is negative, i.e.:

$$\lambda_2(\mathbf{S}^2 + \mathbf{\Omega}^2) < 0 \tag{7}$$

which corresponds to a pressure minimum. Okubo [26] and Weiss [48] independently developed a criterion for divergence-free flows, which is the 2D counterpart to the Q-criterion of Hunt [17]:

$$Q = \frac{1}{2}\left(\|\mathbf{\Omega}\|^2 - \|\mathbf{S}\|^2\right) > 0 \tag{8}$$

Kasten et al. [19], [20] extracted Galilean invariant vortex regions by the use of acceleration $\mathbf{a}$.

2.1.2 Objective Methods

Current state-of-the-art feature extractors aspire to be *objective*, [10], [15], [16]. In continuum mechanics, objectivity refers to the invariance of a measure under a change of the reference frame that transforms a point $(\mathbf{x},t)$ in space-time to a new point $(\mathbf{x}^*,t^*)$ by

$$\mathbf{x}^* = \mathbf{Q}(t)\,\mathbf{x} + \mathbf{c}(t) \quad , \quad t^* = t - a \tag{9}$$

where $\mathbf{Q} \in SO(3)$ is a rotation matrix that is in the group of all rotations about the origin of the Euclidean space $\mathbb{R}^3$, $\mathbf{c}$ is a translation vector, and a is a constant. We assume $\mathbf{Q}$ and $\mathbf{c}$ to be smooth functions of t, cf. [46]. While objectivity proved useful for vortex extraction [10], [16], we introduce even stronger classes of reference frame invariance, which we name *hyper-objective*.

The strain rate tensor $\mathbf{S}$ is one of the few objective differential properties of a vector field, cf. [10], [14]. Haller [14] proposed the M_z criterion, which defines a vortex as a set of fluid trajectories along which the strain acceleration tensor is indefinite over directions of zero strain. For this, he derived a criterion to decide whether a particle is in a non-hyperbolic region, which is checked along particle trajectories, assuming that long-term non-hyperbolic behavior is an indicator for a vortex. Recently, Lagrangian Coherent Structures (LCS) [15] have been computed objectively. A subclass are elliptic LCS, which are nested closed curves that preserve arc length and area in incompressible 2D flows. Haller [15] considered the outermost elliptic LCS as the boundary of a coherent vortex. A Eulerian perspective was chosen by Serra and Haller [39], who extracted objective Eulerian vortex boundaries as closed instantaneous (per time step) curves across which the averaged material stretching rate shows no leading-order variability. They used these (instantaneous) curves to forecast the persistence of a vortex over time [38].

Drouot and Lucius [8] computed an objective counterpart to the Galilean invariant vorticity tensor $\mathbf{\Omega}$. They named it the *relative vorticity tensor* $\widetilde{\mathbf{\Omega}}$, which considers the vorticity in strain basis: $\widetilde{\mathbf{\Omega}} = \mathbf{\Omega} - \mathbf{W}$. Thereby, the rate-of-rotation tensor $\mathbf{W}$ is given

by: $\mathrm{D}\mathbf{e}_i/\mathrm{D}t = \mathbf{W}\,\mathbf{e}_i$, with $\mathbf{e}_i$ being the unit eigenvectors of $\mathbf{S}$ and $\mathrm{D}/\mathrm{D}t$ being the material derivative. Tabor and Klapper [42] defined tensor $\widetilde{\mathbf{\Omega}}$ independently and called it *effective rotation*. Its objectivity was proven by Astarita [1], who used this tensor to calculate an index that classifies the domain into extension-like motions and rigid-body-like rotations. With the relative vorticity tensor $\widetilde{\mathbf{\Omega}}$ traditional region-based methods can be made objective, simply by replacing vorticity tensor $\mathbf{\Omega}$ by $\widetilde{\mathbf{\Omega}}$. An objective counterpart to λ_2 in Eq. (7) is, $\lambda_2(\mathbf{S}^2 + \widetilde{\mathbf{\Omega}}^2) < 0$, cf. Martins et al. [25] and an objective counterpart to the Q criterion in Eq. (8) is, cf. Haller [14]: $[\|\widetilde{\mathbf{\Omega}}\|^2 - \|\mathbf{S}\|^2]/2 > 0$. See Thompson [44] for a recent review of latest advances in this area.

Haller et al. [16] recently took a continuum dynamics perspective. Based on a derivation starting from a dynamic polar decomposition of the deformation gradient, they eventually observed that the subtraction of any two vorticity values $\boldsymbol{\omega}(\mathbf{x}_1, t) - \boldsymbol{\omega}(\mathbf{x}_2, t)$ is objective, which led them to define *relative* vorticity measures. They introduced the instantaneous vorticity deviation (IVD), which subtracts the spatial mean of vorticity in a local neighborhood $U \subseteq D$. A Lagrangian extension that considers the temporal evolution of this measure is the Lagrangian-averaged vorticity deviation (LAVD), which is computed by integrating IVD along a pathline. Note that the value-range of both methods depends on the neighborhood size. Vorticity was reported to produce false-positives in shear flows [32], which need to be removed in a post-process, e.g., by only considering closed vorticity iso-lines with a notable maximum inside. Lugt [24] noted that a local vorticity extremum is not necessary for the existence of a vortex.

2.2 Line-based Methods

While there is no universal definition of a vortex region, the line that all particles rotate around is commonly referred to as vortex coreline. To find these corelines, Sujudi and Haimes [41] formulated the reduced velocity criterion: $\mathbf{v} - (\mathbf{v}^{\mathrm{T}}\mathbf{e})\mathbf{e} = \mathbf{0}$, which says that the projection of the flow vector $\mathbf{v}$ along the eigenvector $\mathbf{e}$ with real-valued eigenvalue gives zero. In other words, the flow is tangential to this eigenvector and exactly on the coreline, there is no swirling motion. Peikert and Roth [28] introduced the parallel vectors operator $||$ to rephrase this as $\mathbf{v} \,||\, \mathbf{J}\,\mathbf{v}$, which avoids explicit computation of the eigenvectors. The above mentioned methods only work in steady flows and they are not Galilean invariant in 3D. A Galilean invariant extension was presented by Weinkauf et al. [47], who identified swirling motion in unsteady flow, using:

$$\text{2D: } \mathbf{v} - \mathbf{f} = \mathbf{0} \qquad \text{3D: } \mathbf{J}(\mathbf{v} - \mathbf{f}) \parallel \mathbf{v} - \mathbf{f} \tag{10}$$

where $\mathbf{f} = -\mathbf{J}^{-1}\,\mathbf{v}_t$ is the feature flow field [43], see Eq. (5). Several other coreline extractors have been introduced in the flow visualization literature. Kasten et al. [19], [20] used the notion of vanishing acceleration $\mathbf{a} = \mathbf{0}$, which is in 2D identical to Eq. (10). Recently, they extended their method to 3D flows [21]. Sahner et al. [34] extracted extremum lines of the region-based methods λ_2 and Q, which was followed by Schafhitzel et al. [36], who considered the topology of λ_2-based vortex corelines. Later, Sahner et al. [35] computed vortex and strain skeletons as extremal structures of M_z. Roth and Peikert [33] extracted bent corelines using a higher-order method. Günther et al. [11] proposed a general approach to transform any Galilean invariant method into a rotation invariant one. Bujack et al. [5] proposed to analyze the extrema of the determinant of $\mathbf{J}$. The approach of Bujack et al. [5] does not involve the temporal derivative and is therefore not equivalent to any of the above Galilean invariant methods.

2.3 Selection of Reference Frame

Instead of finding vortex definitions that are invariant under certain types of reference frame transformations, some techniques try to determine a suitable reference frame.

2.3.1 Vector Field Decomposition

For simple cases, a suitable reference frame can be found by subtraction of a mean flow or a certain percentage of the inflow velocity, which is set by domain experts by experience. Wiebel et al. [49] proposed to subtract the harmonic component of a flow decomposition. Harmonic flows are by definition divergence-free and curl-free, and thus their subtraction does not alter the local divergence and rotation properties. A common flow decomposition is the Helmholtz-Hodge decomposition (HHD), which decomposes a vector field into a scalar potential (curl-free), a vector potential (divergence-free) and a harmonic vector field. See Bhatia et al. [3] for a survey on the HHD. In order to extract vortices, Bhatia et al. [4] introduced their natural HHD. It should be noted, however, that the subtraction of a harmonic part cannot capture rotational movements, as it is always irrotational. Aside from using the HHD to change the reference frame, vortices were identified as extremal structures of the magnitude of the divergence-free part [45].

2.3.2 Optimization-based Measures

The importance of the reference frame has been recognized already in the 70s, e.g., by Lugt et al. [24], who characterized vortices as a fluid moving around a common axis, which can be described by closed or spiraling streamlines if a reference frame exists for which the flow field becomes steady. Similarly, Robinson [32] considered vortices as instantaneous streamlines that exhibit a roughly circular or spiral pattern, when viewed from a reference frame moving with the center of the vortex core. Both definitions are equivalent, since from the perspective moving with the vortex, the flow becomes steady. However, Lugt [24] noted that in unsteady flows there is no *global* reference frame in which the entire flow appears steady, since vortices might move in different directions, making it impossible to follow all vortices at the same time. Perry and Chong [29] noted that for certain flows, e.g., jets in cross-flow, vortices accelerate and become steady in different frames. For this reason, Günther et al. [10] did not seek for a global (spatially-constant) reference frame, but for a *local* one, which allowed them to follow the vortices individually. They estimated an optimal local reference frame for every point $(\mathbf{x}, t)$ in which the transformed velocity field is as steady as possible in a local neighborhood around $(\mathbf{x}, t)$. They limited the reference frame transformation to rotations and translations and have shown that the optimal parameters (angle and offset) can be found by solving a linear problem. For any rotation and translation of the reference frame that can be applied to the input data, their method computes the same distinguished local reference frame. All techniques applied in this frame, therefore become independent of rotations and translations of the input. Hence, standard vortex measures such as Sujudi-Haimes [41] and λ_2 [18] become objective in the optimal frame. Since the transformation into the optimal reference frame was restricted to rotations and translations, the approach did not include (non-)uniform scale or shear. Therefore, deforming vortices might not be captured well, which can occur near boundaries.

3 Optimal Reference Frames

In this paper, we extend the optimization-based method of Günther et al. [10] by investigating different degrees of freedom for

optimal reference frame transformations. In Section 3.1, we begin with the most general case, which is the invariance under affine transformations of the observer. Afterwards in Sections 3.2–3.4, we gradually decrease the number of degrees of freedom until we arrive at the well-known class of Galilean invariance.

3.1 Affine Invariance

To introduce the most general case, we propose the invariance under smooth affine transformations of the reference frame. For this, we consider transformations of the form:

$$\mathbf{x}^* = \mathbf{R}(t)\,\mathbf{x} + \mathbf{c}(t) \quad , \quad t^* = t - a \tag{11}$$

where $\mathbf{R}(t)$ is a general invertible matrix, $\mathbf{c}(t)$ is a translation vector and a is a constant. Affine invariance is formally defined:

Definition 1. A scalar s is affine invariant if it remains unchanged under any change of the reference frame as in Eq. (11). A vector $\mathbf{r}$ is affine invariant if Eq. (11) transforms it to $\mathbf{r}^* = \mathbf{R}(t)\,\mathbf{r}$. A second-order tensor $\mathbf{T}$ is affine invariant if Eq. (11) transforms it to $\mathbf{T}^* = \mathbf{R}(t)\,\mathbf{T}\,\mathbf{R}(t)^{-1}$.

Applying Eq. (11) transforms the vector field into the new frame, which gives $\mathbf{v}^*$, $\mathbf{J}^*$, $\mathbf{a}^*$ and $\mathbf{v}_t^*$, see Appendix A.

Similar to [10], we estimate an optimal reference frame *locally* for every point $(\mathbf{x},\, t)$. The local frame $(\mathbf{R}(t),\, \mathbf{c}(t))$ is chosen such that the transformed velocity field becomes as steady as possible in a local neighborhood U around $(\mathbf{x},\, t)$, i.e., the temporal derivative of the transformed field is minimized:

$$\int_U \|\mathbf{v}_t^*\|^2 dV \rightarrow \min\,. \tag{12}$$

In the following, we denote $\mathbf{R}(t)$ as $\mathbf{R}$ for brevity. We minimize Eq. (12) locally: We locally assume that $\mathbf{R}(t)$ and $\mathbf{c}(t)$ are spatially constant and we solve for the optimal frame at each point in space-time *individually*. For this reason, the derivatives of $\mathbf{R}$ and $\mathbf{c}$ cannot be computed by finite differences, and are thus instead computed explicitly. By setting $\mathbf{R}(t) = \mathbf{I}$ and $\mathbf{c}(t) = \mathbf{0}$, we assure that the optimal transformation passes through the point $\mathbf{x}$ at time t[1]. Thus, at every point $(\mathbf{x},\, t)$, we only search for the unknowns $\dot{\mathbf{R}} = \frac{d\mathbf{R}}{dt}$, $\ddot{\mathbf{R}} = \frac{d\dot{\mathbf{R}}}{dt}$, $\dot{\mathbf{c}} = \frac{d\mathbf{c}}{dt}$, $\ddot{\mathbf{c}} = \frac{d\dot{\mathbf{c}}}{dt}$, which contain 12 scalars (angles and offsets) in 2D and 24 in 3D.

Minimizing Eq. (12) is not straightforward, since $\mathbf{v}_t^*$ is non-linear in $\dot{\mathbf{R}}, \ddot{\mathbf{R}}, \dot{\mathbf{c}}, \ddot{\mathbf{c}}$. We found, however, that $\mathbf{v}_t^*$ can be *linearized* by substitution. Instead of solving for $\dot{\mathbf{R}}, \ddot{\mathbf{R}}, \dot{\mathbf{c}}, \ddot{\mathbf{c}}$ directly, we solve for a suitable combination of these unknowns, which are stored in vector $\mathbf{u}$ by rewriting $\mathbf{v}_t^*$ into the *equivalent* form:

$$\mathbf{v}_t^* = \mathbf{R}\,(\mathbf{v}_t - \mathbf{M}\,\mathbf{u})\,. \tag{13}$$

with the 3×24 matrix $\mathbf{M}$ in 3D:

$$\mathbf{M} = (u\mathbf{I} - x\mathbf{J},\ v\mathbf{I} - y\mathbf{J},\ w\mathbf{I} - z\mathbf{J},\ \mathbf{J},\ \mathbf{I},\ x\mathbf{I},\ y\mathbf{I},\ z\mathbf{I}) \tag{14}$$

and the 24-vector of reference frame transformation parameters:

$$\mathbf{u} = \begin{pmatrix} -vec(\mathbf{H}_1) \\ \mathbf{k}_1 \\ -\mathbf{k}_3 \\ -vec(\mathbf{H}_3) \end{pmatrix} \tag{15}$$

1. Not prescribing $\mathbf{R}$ and $\mathbf{c}$ results in a family of minimizers. By setting $\mathbf{R} = \mathbf{I}, \mathbf{c} = \mathbf{0}$, the solution at $\mathbf{x}$ is selected. The other solutions would be transformed by $\mathbf{R}, \mathbf{c}$ and are not affine invariant, which is analogue to [10].

Matrices $\mathbf{H}_1$, $\mathbf{H}_3$ and vectors $\mathbf{k}_1$ and $\mathbf{k}_3$ contain combinations of the unknown reference frame parameters, which are detailed in Appendix A. In 2D, $\mathbf{u}$ is a 12-vector and the 2×12 matrix $\mathbf{M}$ is

$$\mathbf{M} = (u\mathbf{I} - x\mathbf{J}\ ,\ v\mathbf{I} - y\mathbf{J}\ ,\ \mathbf{J}\ ,\ \mathbf{I}\ ,\ x\mathbf{I}\ ,\ y\mathbf{I})\ . \tag{16}$$

Eq. (13) shows that vector field and reference frame are completely separated: $\mathbf{M}$ contains only $\mathbf{v}$ and its derivatives, while all information of the frame is stored in $\mathbf{u}$. The optimal $\mathbf{u}$ is found by minimizing Eq. (12) using Eq. (13), which is the solution of the linear system:

$$\widehat{\mathbf{M}}\,\mathbf{u} = \widehat{\mathbf{y}} \tag{17}$$

$$\text{with} \quad \widehat{\mathbf{M}} = \int_U \mathbf{M}^{\mathrm{T}}\mathbf{M}\,dV \quad , \quad \widehat{\mathbf{y}} = \int_U \mathbf{M}^{\mathrm{T}}\mathbf{v}_t\,dV. \tag{18}$$

Let $\overline{\mathbf{u}} = (-vec(\overline{\mathbf{H}}_1), \overline{\mathbf{k}}_1, -\overline{\mathbf{k}}_3, -vec(\overline{\mathbf{H}}_3))^{\mathrm{T}} = \widehat{\mathbf{M}}^{-1}\,\widehat{\mathbf{y}}$ be the optimal $\mathbf{u}$. The new fields in the locally optimal frame are

$$\overline{\mathbf{v}} = \mathbf{v} + \overline{\mathbf{H}}_1\,\mathbf{x} + \overline{\mathbf{k}}_1 \tag{19}$$

$$\overline{\mathbf{J}} = \mathbf{J} + \overline{\mathbf{H}}_1 \tag{20}$$

$$\overline{\mathbf{v}}_t = \mathbf{v}_t - \mathbf{M}\,\overline{\mathbf{u}} \tag{21}$$

$$\overline{\mathbf{a}} = \overline{\mathbf{J}}\,\overline{\mathbf{v}} + \overline{\mathbf{v}}_t. \tag{22}$$

which follows directly from insertion of $\overline{\mathbf{u}}$ from Eq. (15) into the Eqs. (45)–(48) in Appendix A. Note that we did not need to compute the actual reference frame parameters $\dot{\mathbf{R}}, \ddot{\mathbf{R}}, \dot{\mathbf{c}}, \ddot{\mathbf{c}}$ directly. Instead, we only needed to determine suitable combinations of them that were stored in $\mathbf{u}$. We refer to Appendix B for a proof that the vector field in the optimal frame $\overline{\mathbf{v}}$ and its derivatives $\overline{\mathbf{J}}$, $\overline{\mathbf{v}}_t$, $\overline{\mathbf{a}}$ are affine invariant.

3.2 Similarity Invariance

In vision, transformations that include rotation, translation and uniform scale are known as similarity transformations. Formally:

$$\mathbf{x}^* = s(t)\,\mathbf{Q}(t)\,\mathbf{x} + \mathbf{c}(t) \quad , \quad t^* = t - a \tag{23}$$

where $\mathbf{Q}(t) \in SO(3)$ is a rotation matrix, $s(t)$ is a positive scalar, $\mathbf{c}(t)$ is a translation vector, and a is a constant. We assume $\mathbf{Q}(t)$, $s(t)$, $\mathbf{c}(t)$ to be smooth functions of t and denote them as $\mathbf{Q}$, s, $\mathbf{c}$. The temporal derivative of the transformed vector field is:

$$\mathbf{v}_t^* = \mathbf{Q}\,(\mathbf{v}_t - \mathbf{M}\,\mathbf{u}) \tag{24}$$

In 3D, $\mathbf{u} = (\mathbf{u}_1, \mathbf{u}_2, \mathbf{u}_3, \mathbf{u}_4, u_5, u_6)$ is a 14-vector. With $\mathbf{X} = sk(\mathbf{x})$ and $\mathbf{V} = sk(\mathbf{v})$, the 3×14 matrix $\mathbf{M}$ can be written as:

$$\mathbf{M} = (-\mathbf{J}\,\mathbf{X} + \mathbf{V}\ ,\ \mathbf{J}\ ,\ \mathbf{X}\ ,\ \mathbf{I}\ ,\ -\mathbf{J}\,\mathbf{x} + \mathbf{v}\ ,\ \mathbf{x})\ . \tag{25}$$

In 2D, $\mathbf{M}$ is a 2×8 matrix

$$\mathbf{M} = (-\mathbf{J}\,\mathbf{x}_p + \mathbf{v}_p\ ,\ \mathbf{J}\ ,\ \mathbf{x}_p\ ,\ \mathbf{I}\ ,\ -\mathbf{J}\,\mathbf{x} + \mathbf{v}\ ,\ \mathbf{x}) \tag{26}$$

with $\mathbf{x}_p = (-y, x)^{\mathrm{T}}$, $\mathbf{v}_p = (-v, u)^{\mathrm{T}}$, and $\mathbf{u}$ is an 8-vector. Note that $\mathbf{u}_1$ and $\mathbf{u}_3$ are scalars in 2D. Let $\overline{\mathbf{u}} = (\overline{\mathbf{u}}_1, \overline{\mathbf{u}}_2, \overline{\mathbf{u}}_3, \overline{\mathbf{u}}_4, \overline{u_5}, \overline{u_6})^{\mathrm{T}}$ be the optimal $\mathbf{u}$ that solves Eq. (17). Then, the new fields in the locally optimal reference frame are

$$\overline{\mathbf{v}} = \mathbf{v} + sk(\overline{\mathbf{u}}_1)\,\mathbf{x} - \overline{u_5}\,\mathbf{x} + \overline{\mathbf{u}}_2 \tag{27}$$

$$\overline{\mathbf{J}} = \mathbf{J} + sk(\overline{\mathbf{u}}_1) - \overline{u_5}\,\mathbf{I}\,. \tag{28}$$

$\overline{\mathbf{v}}_t$ and $\overline{\mathbf{a}}$ follow directly from $\overline{\mathbf{v}}$ and $\overline{\mathbf{J}}$ as in Eqs. (21) and (22). We refer to Appendix C for a derivation of Eqs. (25)–(28).

3.3 Objectivity

We briefly report the findings of Günther et al. [10]. They applied rotations and translations to obtain objective measures, cf. Eq. (9). The temporal derivative of the transformed vector field is:

$$\mathbf{v}_t^* = \mathbf{Q}\,(\mathbf{v}_t - \mathbf{M}\,\mathbf{u}) \tag{29}$$

In 3D, $\mathbf{u} = (\mathbf{u}_1, \mathbf{u}_2, \mathbf{u}_3, \mathbf{u}_4)$ is a 12-vector. With $\mathbf{X} = sk(\mathbf{x})$ and $\mathbf{V} = sk(\mathbf{v})$, the 3×12 matrix $\mathbf{M}$ is:

$$\boxed{\mathbf{M} = (-\mathbf{J}\,\mathbf{X} + \mathbf{V}\ ,\ \mathbf{J}\ ,\ \mathbf{X}\ ,\ \mathbf{I})\ .} \tag{30}$$

In 2D, $\mathbf{M}$ is a 2×6 matrix

$$\boxed{\mathbf{M} = (-\mathbf{J}\,\mathbf{x}_p + \mathbf{v}_p\ ,\ \mathbf{J}\ ,\ \mathbf{x}_p\ ,\ \mathbf{I})} \tag{31}$$

with $\mathbf{x}_p = (-y, x)^{\mathrm{T}}$, $\mathbf{v}_p = (-v, u)^{\mathrm{T}}$, and $\mathbf{u}$ is a 6-vector. As with similarity invariance, $\mathbf{u}_1$ and $\mathbf{u}_3$ are scalars in 2D. Let $\overline{\mathbf{u}} = (\overline{\mathbf{u}}_1, \overline{\mathbf{u}}_2, \overline{\mathbf{u}}_3, \overline{\mathbf{u}}_4)^{\mathrm{T}}$ be the optimal $\mathbf{u}$ that solves Eq. (17). Then, the new fields in the locally optimal reference frame are

$$\boxed{\begin{aligned} \overline{\mathbf{v}} &= \mathbf{v} + sk(\overline{\mathbf{u}}_1)\,\mathbf{x} + \overline{\mathbf{u}}_2 && (32)\\ \overline{\mathbf{J}} &= \mathbf{J} + sk(\overline{\mathbf{u}}_1)\ . && (33) \end{aligned}}$$

$\overline{\mathbf{v}}_t$ and $\overline{\mathbf{a}}$ follow directly from $\overline{\mathbf{v}}$ and $\overline{\mathbf{J}}$ as in Eqs. (21) and (22).

3.4 Galilean invariance

Finally, we derive the optimal reference frame among all Galilean reference frame transformations. This leads to Galilean invariance, which is the invariance under equal-speed translations, see Eq. (6). Using Eq. (48) with $\mathbf{R}(t) = \mathbf{I}$ and $\mathbf{c}(t) = \mathbf{c}_0 + t\ \mathbf{c}_1$, this gives

$$\mathbf{v}_t^* = \mathbf{v}_t - \mathbf{M}\,\mathbf{u} \tag{34}$$

with $\mathbf{M} = \mathbf{J}$ and $\mathbf{u} = \mathbf{c}_1$. For Eq. (34), $\mathbf{v}_t^* = \mathbf{0}$ has a local closed-form solution (no neighborhood U needed) for unknown $\mathbf{u}$:

$$\mathbf{u} = \mathbf{J}^{-1}\mathbf{v}_t \tag{35}$$

which gives the new optimal fields

$$\boxed{\begin{aligned} \overline{\mathbf{v}} &= \mathbf{v} + \mathbf{u} && (36)\\ \overline{\mathbf{J}} &= \mathbf{J}. && (37) \end{aligned}}$$

Note that with $\mathbf{f} = -\mathbf{J}^{-1}\mathbf{v}_t$, the subtraction of the feature flow field $(\mathbf{v} - \mathbf{f})$ is identical to Eq. (36) with Eq. (35). The subtraction of the feature flow field is an approach that was previously proposed by Weinkauf et al. [47] to extract vortices in unsteady flows, see Eq. (10). This sheds new light on their solution: The subtraction of the feature flow field locally transforms the vector field into the most-steady reference frame among all equal-speed translating references frames. Thus this is proof that, if vortices perform equal-speed translations, their method finds the optimal frame.

4 Optimal Flow Decomposition

Above, we described methods to calculate an optimal reference frame for a given class of possible reference frame transformations. By rearranging the expressions of the optimal vector fields in Eqs. (19), (27), (32) and (36), we can see that any given vector field $\mathbf{v}$ can be decomposed into two fields $\overline{\mathbf{v}}$ and $\widetilde{\mathbf{v}}$, see Fig. 2:

$$\mathbf{v} = \overline{\mathbf{v}} + \widetilde{\mathbf{v}} \tag{38}$$

Here, $\overline{\mathbf{v}}$ contains the vector field in the near-steady local reference frame and $\widetilde{\mathbf{v}}$ contains the ambient transport. This decomposition is generally possible, which was previously shown only for the special case of objectivity [10]. The ambient part $\widetilde{\mathbf{v}}$ shows the spatial smoothness of the ambient motion, which reveals the spatial smoothness of the optimal reference frame. In the next section, we use the optimal near-steady reference frame to extract vortices.

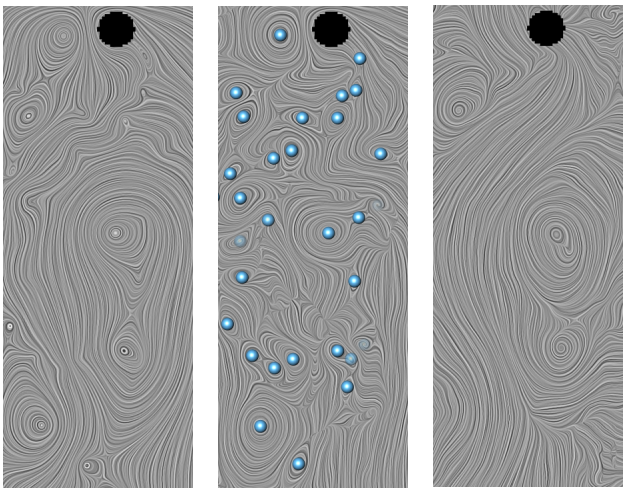

original $\mathbf{v}$ = near-steady $\overline{\mathbf{v}}$ + ambient $\widetilde{\mathbf{v}}$

Fig. 2: Vector field decomposition in the BOUSSINESQ flow. The original field $\mathbf{v}$ is decomposed into a near-steady part $\overline{\mathbf{v}}$ that shows vortices, and an ambient part $\widetilde{\mathbf{v}}$ that depicts the reference frame movement. Here, shown for affine invariance, using $U = 21^2$.

5 Vortices in Optimal Reference Frames

The previous sections demonstrated how any vector field can be locally transformed into a distinguished optimal reference frame and how this leads to an optimal flow decomposition. Among all reference frame transformations of a certain type, e.g., affine transformations, the one is chosen in which the temporal derivative is minimized. Any affine transformation of the input field will be removed by our optimization, thus all measures that are computed in the optimal frame become affine-invariant, i.e., invariant under affine transformations of the observer.

Same as [10], we apply standard vortex measures in the optimal frame using the optimal vector field $\overline{\mathbf{v}}$ and its derivatives $\overline{\mathbf{J}}, \overline{\mathbf{v}}_t, \overline{\mathbf{a}}$.

Vortex Corelines

A necessary condition for swirling motion is the presence of complex eigenvalues in the Jacobian $\overline{\mathbf{J}}$. In 2D, optimal vortex corelines can be tracked as paths of critical points in $\overline{\mathbf{v}}$ and in 3D, optimal vortex corelines can be extracted by applying Sujudi-Haimes [41] with the parallel vectors operator [28]:

$$\text{2D: } \overline{\mathbf{v}} = \mathbf{0} \qquad \text{3D: } \overline{\mathbf{J}}\overline{\mathbf{v}} \parallel \overline{\mathbf{v}} \tag{39}$$

These techniques usually only work in steady flows. Since we observe unsteady flows in the optimal near-steady reference frame, our method extracts the vortex corelines of pathlines.

Vortex Regions

In the optimal reference frame, region-based methods such as λ_2 can be applied as well. Using the optimal Jacobian matrix $\overline{\mathbf{J}}$, we compute a new optimal vorticity tensor $\overline{\mathbf{\Omega}}$. Using this, we define a new (hyper-)objective $\overline{\lambda}_2$ measure:

$$\overline{\lambda}_2(\mathbf{S}^2 + \overline{\mathbf{\Omega}}^2) < 0 \qquad \text{with} \qquad \overline{\mathbf{\Omega}} = \frac{\overline{\mathbf{J}} - \overline{\mathbf{J}}^{\mathrm{T}}}{2} \tag{40}$$

In previous work, Günther et al. [10] also considered other region-based methods such as vorticity in the optimal frame, which is analogue for the hyper-objective methods. In fact, any vortex measure that is based on velocity and its derivatives can be observed in an optimal reference frame using our method.

6 Implementation

Our method is a pre-process prior to standard flow visualization techniques. Thus, it fits well into existing visualization pipelines. We implemented our method as a vtkImageAlgorithm filter for VTK [37], which is included for the 2D case in the supplemental material. The input to our method is an unsteady vector field $\mathbf{v}(\mathbf{x}, t)$ and the output are the vector field $\overline{\mathbf{v}}$ and its derivatives $\overline{\mathbf{J}}$, $\overline{\mathbf{v}}_t$, $\overline{\mathbf{a}}$ in the optimal reference frame. The computation of the optimal reference frame is local and easy to parallelize, since each voxel is processed independently in both space and time. The algorithm requires to iterate the data set twice, which is shown in Alg. 1 for the 2D case. The algorithm is analogue for 3D domains.

First Pass: Discretization and Summed Area Tables

Our method requires a discretization of the domain. On numerical data, we use the grid on which the flow was simulated or measured. For analytic flows, we subdivide the domain uniformly into 2–8 million voxels, depending on the data set.

To setup the linear system, we compute $\mathbf{M}$ at each grid point. The computation of $\mathbf{M}$ depends on the chosen type of reference frame invariance, e.g., Eqs. (14) and (16) for affine invariance. In Section 3, we highlighted the respective formulas for $\mathbf{M}$ with boxes that have the same color as the corresponding corelines that are visualized in the remainder of the paper. Afterwards, we compute for every grid point $\mathbf{M}^{\mathrm{T}}\mathbf{M}$ and $\mathbf{M}^{\mathrm{T}}\mathbf{v}_t$, and generate a *summed area table* (SAT) for both on the fly, which we name $\widehat{\mathcal{M}}$ and $\widehat{\mathcal{Y}}$. SATs are data structures that allow us to efficiently calculate the sum over arbitrary rectangular domains in constant time, which we will use to integrate $\mathbf{M}^{\mathrm{T}}\mathbf{M}$ and $\mathbf{M}^{\mathrm{T}}\mathbf{v}_t$ in a neighborhood U, cf. Eq. (18). A SAT data structure is built in linear time and can be reused for all grid points. Note, however, that SATs are only available on regular grids. If the data is given on unstructured grids, $\mathbf{M}^{\mathrm{T}}\mathbf{M}$ and $\mathbf{M}^{\mathrm{T}}\mathbf{v}_t$ are integrated traditionally by iterating the neighborhood for each grid point, which is linear in the number of grid points inside the neighborhood region and therefore output-sensitive. The remaining steps of the pipeline remain unchanged.

Second Pass: Linear Problem and Optimal Frame

Using the SATs $\widehat{\mathcal{M}}$ and $\widehat{\mathcal{Y}}$, we compute $\widehat{\mathbf{M}}$ and $\widehat{\mathbf{y}}$, which is an $O(1)$ operation, since we only need to look up and combine the SAT values at the corners of the neighborhood region U. Afterwards, we solve $\widehat{\mathbf{M}}\,\mathbf{u} = \widehat{\mathbf{y}}$ for each grid point to compute the optimal reference frame parameters $\overline{\mathbf{u}}$, cf. the linear system in Eq. (17). For this, we use a Householder QR decomposition with full-pivoting.

Given the optimal parameters $\overline{\mathbf{u}}$, we compute and store the vector field $\overline{\mathbf{v}}$ and its derivatives $\overline{\mathbf{J}}$, $\overline{\mathbf{v}}_t$, $\overline{\mathbf{a}}$ in the optimal reference frame. Again, the formulas depend on the chosen type of reference frame invariance. We highlighted the formulas throughout Section 3. For affine invariance, we use Eqs. (19)–(22). In the optimal reference frame, we apply standard techniques to compute frame-invariant vortex corelines and vortex regions, cf. Section 5.

Input : unsteady flow $\mathbf{v}(\mathbf{x}, t)$, time τ, neighborhood U
Output : flow in optimal frame $\overline{\mathbf{v}}$ and derivatives $\overline{\mathbf{J}}$, $\overline{\mathbf{v}}_t$, $\overline{\mathbf{a}}$

// initialize arrays for SATs
$\{\widehat{\mathcal{M}}_{i,j}\} \leftarrow \mathbf{0}, \quad \{\widehat{\mathcal{Y}}_{i,j}\} \leftarrow \mathbf{0}$;

// for each grid point: compute $\mathbf{M}$, $\mathbf{y}$ and SAT
forall (i, j) **do**
  $\mathbf{M} \leftarrow$ Eq. (14) ; // with $\mathbf{v}(\mathbf{x}_{i,j}, \tau)$, $\mathbf{J}(\mathbf{x}_{i,j}, \tau)$
  $\mathbf{y} \leftarrow \frac{\partial}{\partial t}\mathbf{v}(\mathbf{x}_{i,j}, \tau)$;
  // compute SATs
  $\widehat{\mathcal{M}}_{i,j} \leftarrow \mathbf{M}^{\mathrm{T}}\mathbf{M} + \widehat{\mathcal{M}}_{i-1,j} + \widehat{\mathcal{M}}_{i,j-1} - \widehat{\mathcal{M}}_{i-1,j-1}$;
  $\widehat{\mathcal{Y}}_{i,j} \leftarrow \mathbf{M}^{\mathrm{T}}\mathbf{y} + \widehat{\mathcal{Y}}_{i-1,j} + \widehat{\mathcal{Y}}_{i,j-1} - \widehat{\mathcal{Y}}_{i-1,j-1}$;
end

// for each grid point: setup system and solve
forall (i, j) **do**
  // compute neighborhood sum from SAT
  $\widehat{\mathbf{M}} \leftarrow \widehat{\mathcal{M}}_{i+U,j+U} + \widehat{\mathcal{M}}_{i-U-1,j-U-1} - \widehat{\mathcal{M}}_{i+U,j-U-1} - \widehat{\mathcal{M}}_{i-U-1,j+U}$
  $\widehat{\mathbf{y}} \leftarrow \widehat{\mathcal{Y}}_{i+U,j+U} + \widehat{\mathcal{Y}}_{i-U-1,j-U-1} - \widehat{\mathcal{Y}}_{i+U,j-U-1} - \widehat{\mathcal{Y}}_{i-U-1,j+U}$;
  // linearly solve for parameters
  $\overline{\mathbf{u}} \leftarrow \widehat{\mathbf{M}} \setminus \widehat{\mathbf{y}}$;
  // compute optimal frame
  $\overline{\mathbf{v}} \leftarrow$ Eq. (19) ; // with $\overline{\mathbf{u}}$, $\mathbf{v}(\mathbf{x}_{i,j}, \tau)$
  $\overline{\mathbf{J}} \leftarrow$ Eq. (20) ; // with $\overline{\mathbf{u}}$, $\mathbf{J}(\mathbf{x}_{i,j}, \tau)$
  $\overline{\mathbf{v}}_t \leftarrow$ Eq. (21) ; // with $\mathbf{M}_{i,j}$, $\overline{\mathbf{u}}$, $\mathbf{v}_t(\mathbf{x}_{i,j}, \tau)$
  $\overline{\mathbf{a}} \leftarrow \overline{\mathbf{J}}\overline{\mathbf{v}} + \overline{\mathbf{v}}_t$
end

Algorithm 1: For an unsteady vector field $\mathbf{v}(\mathbf{x}, t)$ and time τ, we compute the optimal reference frame $\overline{\mathbf{v}}$ and its derivatives $\overline{\mathbf{J}}$, $\overline{\mathbf{v}}_t$. The algorithm is shown for affine invariance and is the same for similarity invariance and objectivity, when using the respective equations for $\mathbf{M}$ and $\overline{\mathbf{v}}$, $\overline{\mathbf{J}}$, $\overline{\mathbf{v}}_t$, $\overline{\mathbf{a}}$ from Section 3.

7 Results

In the following, we compare Galilean invariant, objective and hyper-objective (similarity invariant and affine invariant) techniques in terms of energy residual, numerical robustness and extraction time. In 2D, the extraction time for the entire space-time volume is measured. In 3D, the time is measured for a single time step.

7.1 Analytic 2D Flows

First, we systematically test our method in a number of analytic 2D vector fields, which contain various vortex movements. When increasing the complexity of the vortex movement, the frame invariant techniques will one-by-one start to fail. Affine invariance is the most general method and will be able to handle all cases.

7.1.1 Four Rotating Centers (Objectivity)

As soon as a vortex moves on a non-linear path, such as on a circle, Galilean invariant methods [12], [21], [47] do not work anymore. This can be seen in the Four Centers flow in Fig. 3. Günther et al. [11] defined the steady flow in the domain $D = [-2, 2]^2$:

$$\mathbf{v}(x, y) = \begin{pmatrix} -x(2y^2 - 1)e^{-x^2-y^2} \\ y(2x^2 - 1)e^{-x^2-y^2} \end{pmatrix} \tag{41}$$

which contains two CW-rotating vortices at $(\pm 2^{-1/2}, \pm 2^{-1/2})$ and two CCW-rotating vortices at $(\pm 2^{-1/2}, \mp 2^{-1/2})$. We observe the flow for time $T = [0, 2\pi]$ in a reference frame that rotates CCW with unit speed around the origin $\mathbf{x}_0 = \mathbf{0}$. We discretized

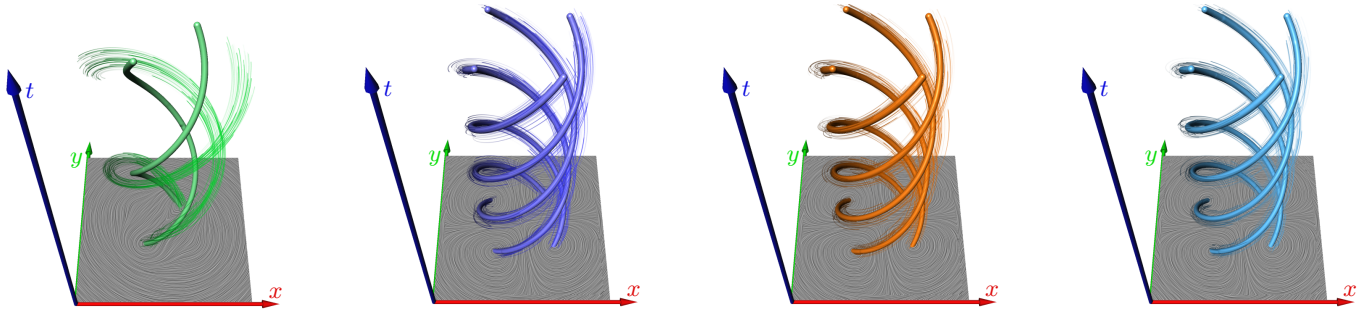

Average residual: 0 (local)
Computation time: 0.68 s

(a) Galilean invariance ✗

Average residual: 4.23×10^{-4}
Average condition: 1.62×10^{5}
Computation time: 7.29 s

(b) Objectivity ✓

Average residual: 3.38×10^{-4}
Average condition: 2.33×10^{5}
Computation time: 11.79 s

(c) Similarity invariance ✓

Average residual: 2.2×10^{-4}
Average condition: 1.7×10^{7}
Computation time: 26.91 s

(d) Affine invariance ✓

Fig. 3: In the FOUR CENTERS flow, vortices rotate with equal speed around a common point. Galilean invariance is not enough. $U = 21^2$.

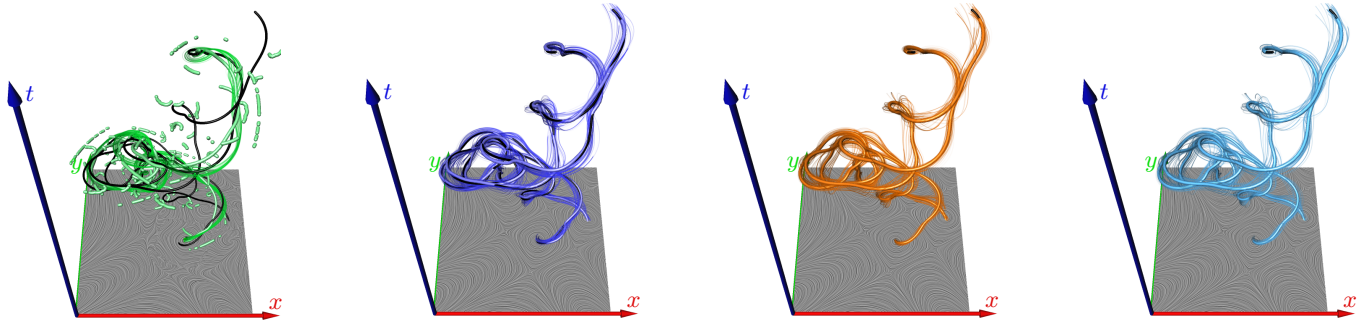

Average residual: 0 (local)
Computation time: 5.12 min

(a) Galilean invariance ✗

Average residual: 2.94
Average condition: 9.79×10^{5}
Computation time: 10.62 min

(b) Objectivity ✗

Average residual: 0
Average condition: 1.22×10^{6}
Computation time: 10.5 min

(c) Similarity invariance ✓

Average residual: 1×10^{-10}
Average condition: 2.17×10^{8}
Computation time: 10.63 min

(d) Affine invariance ✓

Fig. 4: Hyper-objective methods correctly extract vortices in the SIMILARITY HELIX flow. Ground truth is shown in black, $U = 41^2$.

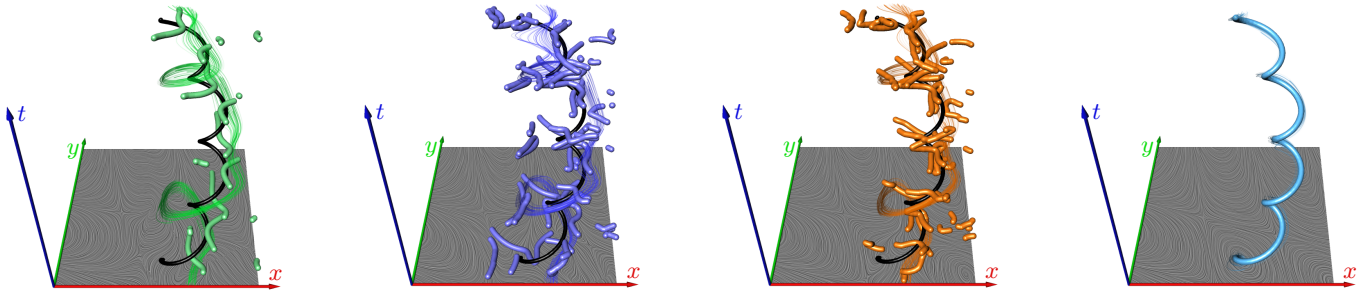

Average residual: 0 (local)
Computation time: 14.6 min

(a) Galilean invariance ✗

Average residual: 28.78
Average condition: 8.01×10^{5}
Computation time: 28.6 min

(b) Objectivity ✗

Average residual: 14.06
Average condition: 1.19×10^{6}
Computation time: 28.88 min

(c) Similarity invariance ✗

Average residual: 1.8×10^{-9}
Average condition: 2.98×10^{9}
Computation time: 29.06 min

(d) Affine invariance ✓

Fig. 5: In the AFFINE HELIX flow, only the affine invariant method finds the correct reference frame. Here, shown for $U = 41^2$.

the transformed vector field onto a regular grid with 128^3 voxels. Compared to the previous and the next two examples, the residual of all but the Galilean invariant method is in the order of 10^{-4}. This deviation from zero stems from the discretization and the numerical finite differences that are needed to setup matrix $\mathbf{M}$. This shows us that, even though this case should have a perfect solution, numerical inaccuracies give us a residual in this order. Visually, these differences are not visible.

7.1.2 *Similarity Helix (Similarity Invariance)*

The next data set is constructed by transforming the co-gradient of the stream function $s(x, y) = 10x(1-x)(1+x)(1/2-y)(1/2+y)$ with the following time-dependent domain transformation:

$$\begin{pmatrix} x^* \\ y^* \end{pmatrix} = \begin{pmatrix} \cos(t) \\ \sin(t) \end{pmatrix} + a(t) \left[x \begin{pmatrix} \cos(4t) \\ \sin(4t) \end{pmatrix} + y \begin{pmatrix} -\sin(4t) \\ \cos(4t) \end{pmatrix} \right] \tag{42}$$

with $a(t) = \sin(10t)/4 + 1$. We refer to [11], [22] for details on domain transformations of vector fields. We visualize the vector field in the spatial domain $D = [-2, 2]^2$ and for time $T = [0, 2\pi]$ in Fig. 4. The space-time domain was discretized onto a $128 \times 128 \times 256$ grid, and we set $U = 41^2$. The ground truth corelines are shown as black curves. The minimizer of the objective method is close to the ground truth, but does not reach it as well as the hyper-objective methods, which can be seen by the residual. The symbolic evaluation of this analytic transformation is quite slow, which led to a computation time that is significantly higher

than the results demonstrated later on numerical vector fields.

7.1.3 Affine Helix (Affine Invariance)

The last example shows a vector field for which only the affine invariant method produces the correct result. The flow is constructed by analytically transforming the co-gradient of the same stream function $s(x, y) = 10x(1 - x)(1 + x)(1/2 - y)(1/2 + y)$, but with the time-dependent domain transformation:

$$\begin{pmatrix} x^* \\ y^* \end{pmatrix} = \begin{pmatrix} \cos(t) \\ \sin(t) \end{pmatrix} + \frac{x}{4} \begin{pmatrix} 3 + \cos(14t) \\ \sin(14t) \end{pmatrix} + \frac{y}{4} \begin{pmatrix} \cos(15t) \\ 3 - \sin(15t) \end{pmatrix} \tag{43}$$

Fig. 5 shows all methods in the spatial domain $D = [-1, 1]^2$ and in the temporal domain $T = [-1, 1]$ for $U = 41^2$. The vector field was discretized onto a space-time grid with 128^3 voxels. As in all other examples, both the condition number and the extraction time increase with higher degree of frame invariance. The Galilean invariant, objective and similarity invariant approach do not find the ground truth coreline, which is shown as black curve.

7.2 Numerical 2D Flows

In the following, we apply our optimization-based vortex coreline extractors to four numerical 2D vector fields.

7.2.1 2D Cylinder

The 2D CYLINDER data set contains a cylinder flow with Reynolds number $Re = 160$ and it is given on an unstructured grid. Behind the obstacle, a von-Kármán vortex street forms. We used VTK to calculate the derivatives, resampled the flow and its derivatives onto a regular grid (160×20) and calculated the optimal frame on the regular grid. In Fig. 6, we show the vortex cores as critical points in the optimal reference frame for all types of frame invariance. For each vortex core we map the swirling strength (magnitude of the imaginary part of the complex-conjugate pair of eigenvalues) to transparency to distinguish between weak and strong vortices. The Galilean invariant method can be expressed as: $\mathbf{v} + \mathbf{J}^{-1}\,\mathbf{v}_t = \mathbf{0}$, cf. Eqs. (35) and (36). The inverse of the Jacobian might be sensitive to noise, depending on the condition of $\mathbf{J}$. A local method such as the Galilean invariant one might therefore produce noisy results, while the other three methods (objectivity, similarity invariance and affine invariance) all have an inherent smoothing due to the neighborhood size $U = 11^2$. The results are visually similar, since vortices move with almost constant speed in a constant direction, which is a kind of movement that is included in all compared invariance classes. However, affine invariance has again the smallest energy residual, as it can compensate for small spatially-varying movement differences, caused by real motion, noise or resampling artifacts.

7.2.2 Boussinesq

The BOUSSINESQ flow contains an unsteady convection simulation that develops around a heated cylinder. The vector field is discretized onto a space-time grid with $100 \times 300 \times 1601$ voxels. As in the example before, we extract the corelines for all methods and map the swirling strength to transparency in Fig. 7. Here, for $U = 21^2$. In this flow, vortices move fairly slowly. The Galilean invariant method is sensitive to noise, whereas the optimization-based approaches give similar results. Only minor differences are observable in the weak vortices. This is explained by the decomposition $\mathbf{v} = \overline{\mathbf{v}} + \widetilde{\mathbf{v}}$ in Eq. (38), which shows that the ambient movement $\widetilde{\mathbf{v}}$ of a vortex adds to the flow structures in $\overline{\mathbf{v}}$ (flow in near-steady frame) to produce the observed field $\mathbf{v}$. If the ambient movement $\widetilde{\mathbf{v}}$ is fast enough, it overshadows the structures in $\overline{\mathbf{v}}$, hiding the features from our view. However, the faster a vortex rotates, i.e., the larger the magnitude of $\overline{\mathbf{v}}$, the smaller is the impact of ambient transport $\widetilde{\mathbf{v}}$. Thus, if vortices move slowly compared to their rotational speed, they are detectable with every class of invariance. As shown in Fig. 7, all optimization-based methods show agreement on stronger vortices. Weak vortices, on the other hand, are easily overshadowed by ambient motion $\overline{\mathbf{v}}$ and for them the right choice of reference frame invariance is crucial. In this example, affine invariance outperforms all other techniques in terms of the lowest energy residual, but this is bought at the expense of an increased condition number and with higher computation time.

7.2.3 Centrifugal Pump

The CENTRIFUGAL PUMP flow contains a numerical simulation with the DES turbulence model. The reference frame rotates with the blades, and the space-time domain was resampled onto a $512 \times 512 \times 80$ grid. We extracted vortex corelines with all optimization-based approaches and visualize them in space-time in Fig. 8 for $U = 21^2$. A common quality measure of vortex corelines [11] is the absolute value of the dot product between normalized coreline tangent and normalized pathline tangent in space-time, since ideally, corelines should follow pathlines. We color-code this tangent alignment and map the swirling strength (imaginary part of complex eigenvalues) to the coreline radius to emphasize strong vortices. Coreline segments with a tangent alignment > 0.1 are removed. Affine invariance produced the best corelines both in terms of tangent alignment and lowest residual.

7.2.4 Moving Obstacle

The MOVING OBSTACLE data set contains a numerical simulation of an incompressible liquid that is confined by a rectangular domain and that is stirred into motion by an obstacle that accelerates and decelerates along a line. In the wake of the obstacle, vortices are created, which are later deformed by the obstacle. In this closed domain, vortices move in different directions, making it necessary to optimize for their respective near-steady reference frames locally. In the presence of more complex obstacle or boundary interactions, vortex deformations are better captured in affine-transformed reference frames, which is evident by the lower residual. This is because of the non-uniform scale and the spatially-varying translation that vortices undergo upon interaction with the obstacle. In Fig. 9, the extracted vortex cores are compared for objectivity, similarity invariance and affine invariance. Differences among the method are visible in areas that are compressed or deformed due to the arrival of the obstacle. The ambient flow is closely related to the movement of the obstacle.

7.3 Parameter Study: Neighborhood U

Next, we elaborate on the size and shape of the neighborhood U.

7.3.1 Size of Neighborhood

To explore the effect of the neighborhood size U, we vary U and observe the average residual and the condition number for all optimization-based approaches in the BOUSSINESQ flow in Fig. 10. The left plot shows that the residual increases when increasing U, which is expected. When fitting the optimal reference transformation to a larger neighborhood U, the fit is not as tight as for a smaller neighborhood, but the solution will be smoother and less prone to noise. Objectivity and similarity invariance are roughly

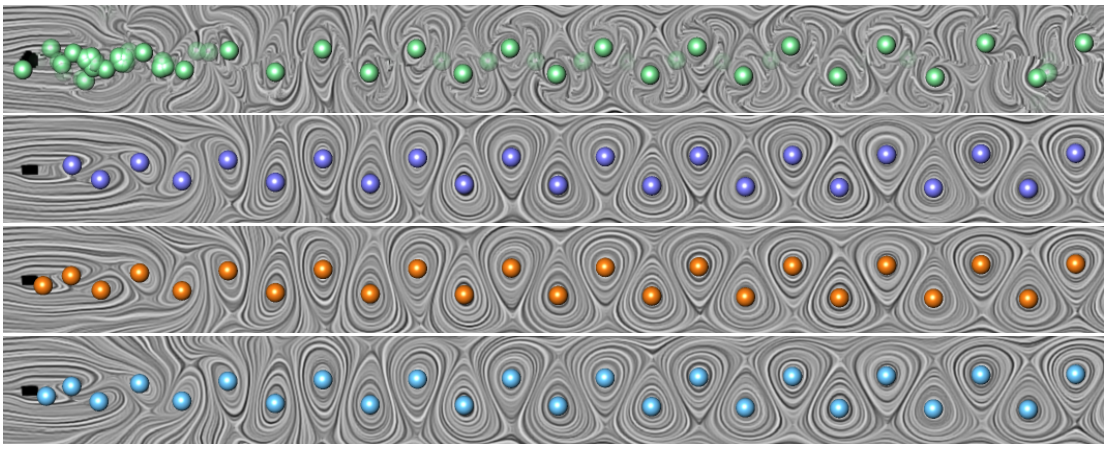

Fig. 6: Galilean invariant, objective and hyper-objective vortex cores in a 2D CYLINDER flow. The swirling strength (imaginary part of eigenvalue) is mapped to transparency to fade out weak vortices. The Galilean invariant method is sensitive to noise. Objective and hyper-objective methods produce visually similar results, but with hyper-objectivity the energy residual is lower. With $U = 11^2$.

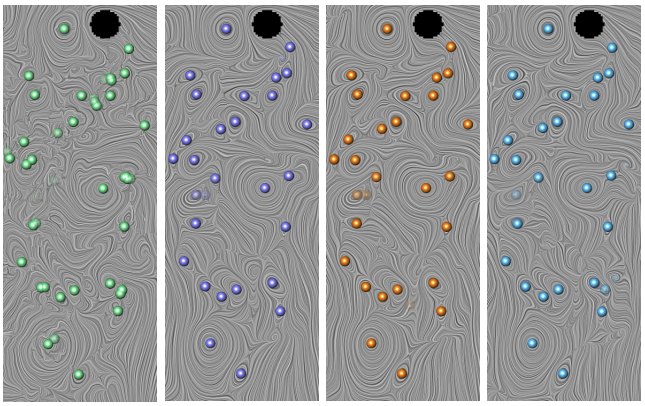

(a) Galilean inv. (b) Objectivity (c) Similarity inv. (d) Affine inv.

Fig. 7: In the BOUSSINESQ, all methods produce visually similar results, with minor differences among weak vortices. The Galilean invariant approach has no inherent smoothing and thus contains noise. In comparison, hyper-objective methods have a significantly smaller residual. For all critical points, the swirling strength (magnitude of imaginary part) is mapped to transparency. $U = 21^2$.

Avg. resid.: 5.047
Avg. cond.: 3.3×10^{9}
Comp. time: 33.19 s
(a) Objectivity

Avg. resid.: 4.325
Avg. cond.: 5.4×10^{9}
Comp. time: 53.40 s
(b) Similarity invariance

Avg. resid.: 2.111
Avg. cond.: 6.6×10^{11}
Comp. time: 130.2 s
(c) Affine invariance

Fig. 8: Space-time visualization of vortex cores in the CENTRIFUGAL PUMP for $U = 21^2$ (time is in view direction). The tangent alignment (angle between vortex coreline and pathline) is color-coded. The coreline radius is scaled by the swirling strength, making strong vortices apparent. Aside from some long-living vortex cores, the results are spurious in this rather turbulent flow, but are quantitatively and qualitatively best with affine invariance.

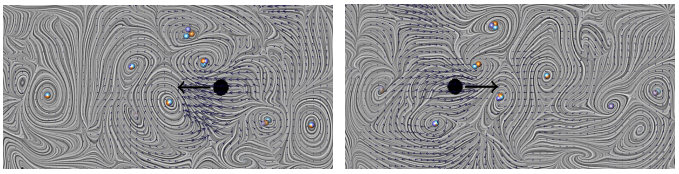

Fig. 9: Two time steps of the MOVING OBSTACLE simulation. The imaginary part of complex eigenvalues is mapped to transparency, $\overline{\mathbf{v}}$ is shown by LIC and $\widetilde{\mathbf{v}}$ is shown by an arrow plot (magnitude scaled by factor 5) for affine invariance. Here, for the local optimized reference frames with $U = 21^2$. The obstacle influences the vortex paths and deforms them. The average residual reduced from 12.02 (objectivity) to 11.41 (similarity) and 7.88 (affine).

in the same order, whereas affine invariance is always significantly better. When increasing U, the condition number decreases, as shown in the right plot, which is also in accordance with our expectation. The more information we have about the neighborhood, the better is the condition of the system. The smoothing by a sufficiently large neighborhood size is important, since the linear system is under-determined at a single point. The more degrees of freedom the unknown reference frame transformation has, the more information we need. Each additional point adds more conditions and we need enough to fill up the rank. Selecting the neighborhood size is a data set-dependent compromise between numerical stability (larger U is better) and low energy residuals (small U is better). Fig. 11 shows the affine invariant vortices and the flow in the optimal reference frame for varying neighborhood sizes U. The extracted vortices are very similar. Though, care should be taken to select U not too small, since then the optimal reference frame might be affected by noise in the data. This does not only include numerical noise or measurement noise, but also resampling artifacts.

The neighborhood should also be chosen in a way such that points that are considered to belong to the same vortex, are observed in a similar reference frame. In other words: the neighborhood size should not contain vortices that move in different directions, i.e., the movement inside the region should be coherent. A visualization of the ambient flow in comparison with the visualization of the obtained optimal reference frame as in Fig. 2 can help to visually guide the selection of the size of the neighborhood region.

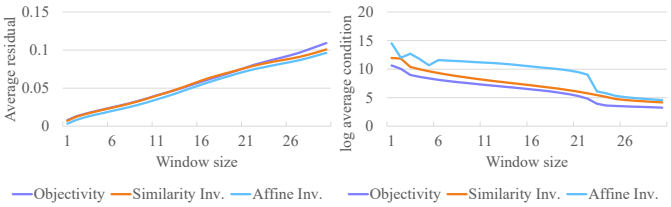

Fig. 10: Residual and condition for various neighborhood sizes U in the BOUSSINESQ flow. With increasing U, the residual increases, since the optimal frame is fit to an entire region. At the same time the condition number improves, since more information is available that makes the system more stable to solve. Affine invariance has the lowest residual, but also the worst condition number, making it numerically less stable than objectivity and similarity invariance.

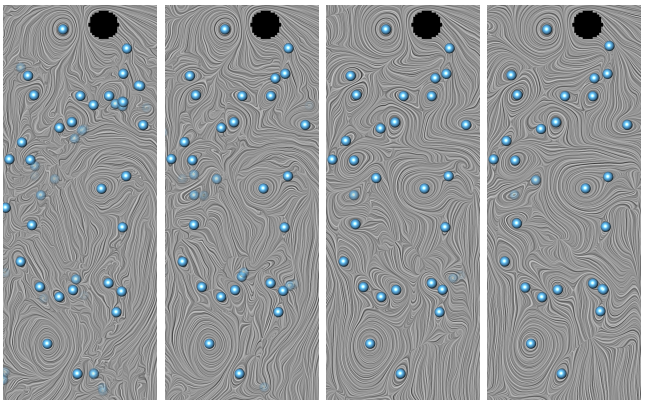

(a) $U = 7^2$ (b) $U = 11^2$ (c) $U = 21^2$ (d) $U = 31^2$

Fig. 11: The size of the neighborhood region U has an influence on the numerical stability (the larger the better). At the same time, a larger neighborhood region U increases the energy residual (the smaller the better). The selection of U is a compromise between numerical stability, sensitivity to noise and locality of the optimal frame. Here, shown for the BOUSSINESQ flow. In all cases, the computation took $2.79\,min$.

7.3.2 Shape of Neighborhood

We explored three different shapes for the neighborhood region U: a square, a rotated square (diamond) and a circle, which are shown in Fig. 12. The circle is the most natural choice, as it resembles the appearance of vortices best. In fact, this shape produced the best (lowest) energy residuals. The difference to (rotated) square shapes, however, is small. A square shape is an attractive alternative, since the integral over the neighborhood region U can be greatly accelerated with the use of summed-area tables (SAT). For the examples in Fig. 12, the summed area table reduced the extraction time down to $15 - 30\%$ for a neighborhood size of $U = 21^2$. The performance difference will increase even further the larger neighborhood U is chosen, since SATs allow for a constant time calculation of an integral, after a one-time linear pre-process.

7.4 Analytic 3D Flow

We constructed an analytic 3D field, in which only the affine invariant method extracts the correct coreline. The underlying steady flow is a 3D extension of the example in Section 7.1.2 with unit flow in the third dimension. The 3D rotation of the reference frame includes a time-dependent shear component, which creates a spatially-varying translation that can only be removed with the affine invariant method. The vector field is discretized onto a 128^3 grid, and the reference frame is optimized for a neighborhood of $U = 81^3$ voxels. Fig. 13 shows the optimization-based corelines for all methods. Objectivity and similarity invariance both produces false-positives ($t = 0$, saturated) and noisy corelines at ($t = 1$, bright colors). Pathlines (gray) are traced to illustrate that only for the affine invariant case, pathlines correctly connect the corelines.

7.5 Numerical 3D Flows

In the following, we describe applications of our method in two numerical 3D data sets.

7.5.1 Square Cylinder

The SQUARE CYLINDER sequence is a numerical simulation in which a von-Kármán vortex street forms behind an obstacle. The spatial domain is discretized onto a $192 \times 64 \times 48$ grid. Fig. 14 shows our optimization-based vortex corelines in this flow for $U = 41^3$. We also refer to the accompanying video for a time series animation. In this flow, vortex corelines move on fairly linear paths. We can therefore expect that Galilean invariance is a good assumption, which is included in all higher invariance classes as special case. Indeed, our optimization-based approaches give all similar results except for the highly bent corelines directly in the wake of the obstacle. In this area, vortices are created and accelerate from zero speed to the downstream velocity. Here, the equal-speed assumption of Galilean invariance does not hold and we can thus expect improvements when searching for time-varying reference frame transformations. In the wake of the obstacle, the affine invariant method favors a coreline that has lower curvature. In turn, less artifacts occurred in the time series.

7.5.2 Swirling Jet

The SWIRLING JET flow contains the periodic spatio-temporal evolution of a turbulent swirling jet undergoing vortex breakdown. This vector field was resampled onto a $201 \times 220 \times 201$ voxel grid. Fig. 15a displays an FTLE field. The in-flow is coming from below in a circular pattern that generates a recirculation bubble. Behind this bubble and in the periphery helical vortex structures arise that are transported down the flow. The Galilean invariant λ_2 in Fig. 15b indicates a vortex tube in the center, which is due to the relative rotation of the entire system. Particles however, are not actually rotating around each other. The objective $\overline{\lambda}_2$ of Günther et al. [10] in Fig. 15c views the flow in the optimal rotating reference frame. In this frame, $\overline{\lambda}_2$ does not detect the vortex tube, indicating that the rotating motion stems from the ambient motion $\widetilde{\mathbf{v}}$ and is not a feature detectable in the steady frame $\overline{\mathbf{v}}$. Our affine-invariant $\overline{\lambda}_2$ in Fig. 15d handles the shear part of the outer vortex helix better, which leads to a helix that aligns better with the FTLE structures. In addition, the last helix loop is better preserved. This is indication for a spatially-varying ambient motion that is only removed by affine invariance. This suggests that optimal reference frames pay off especially in rotating systems that exhibit strong shear effects.

7.6 Discussion

In the following, we elaborate on the physical interpretation, steady flows, turbulent flows, the existance of solutions, the interpretation of the ambient flow, artificial vortices and possible extensions including higher-order methods and Lagrangian vortex measures.

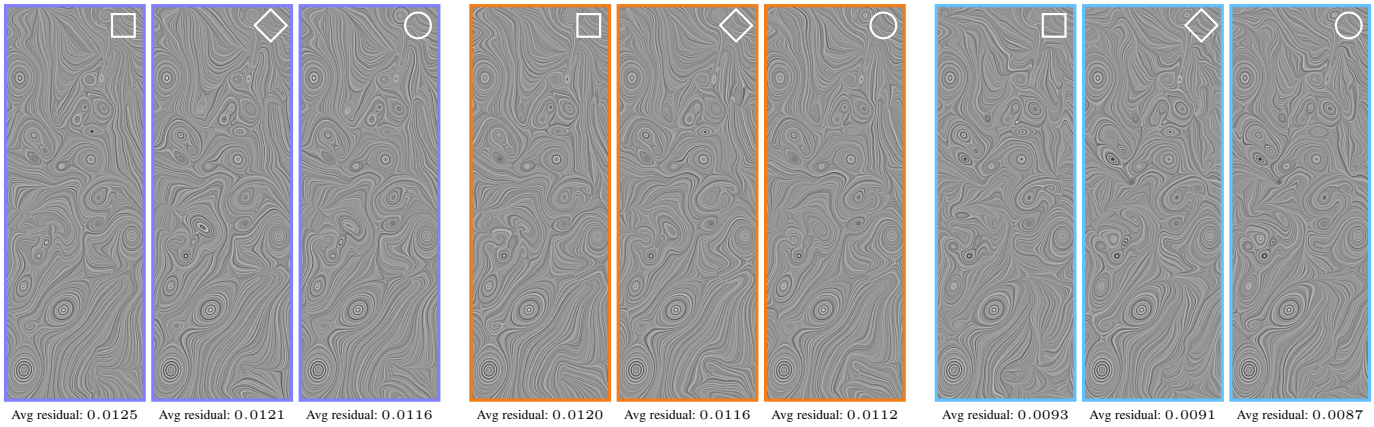

(a) Objectivity (square, diamond, circle) (b) Similarity invariance (square, diamond, circle) (c) Affine invariance (square, diamond, circle)

Fig. 12: The shape of the neighborhood region U has a small effect on the extraction result, as shown here for the BOUSSINESQ flow. We experimented with three different shapes (square, diamond and circle), and report the obtained average residuals. Here, $U = 21^2$.

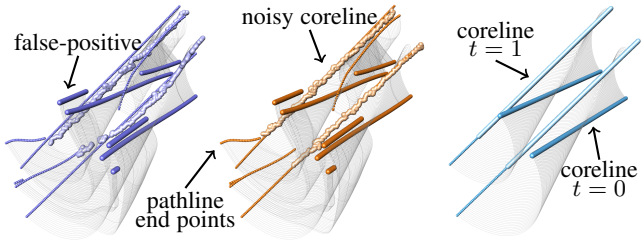

(a) Objectivity (b) Similarity invariance (c) Affine invariance

Fig. 13: Vortex corelines in an ANALYTIC 3D flow, $U = 81^3$. Ideally, pathlines (gray lines) should connect corelines that were extracted at different time steps ($t = 0$ saturated, $t = 1$ bright colors). Only affine invariant corelines are reached exactly. The end points of pathlines (seeded at $t = 0$ and traced until $t = 1$) are shown as small spheres. The objective and similarity-invariant approach extract a number of false-positive corelines at $t = 0$ and produce noisy corelines at $t = 1$.

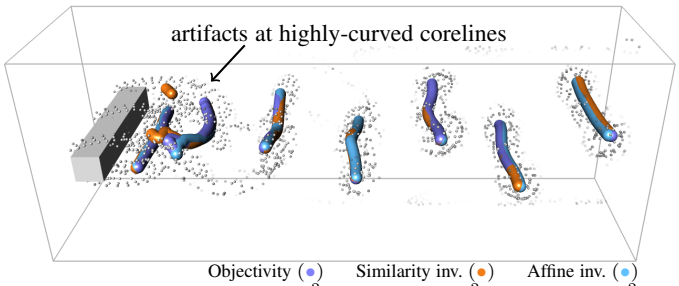

Fig. 14: Objective (•), similarity invariant (•) and affine invariant (•) vortex corelines in the SQUARE CYLINDER flow. In this flow, vortex cores move fairly linear and thus differences are small, except for the highly bent corelines directly in the wake of the cylinder. As a reference, particles are shown in areas of high vorticity, indicating that the corelines are indeed centers of rotating particle motion. $U = 41^3$.

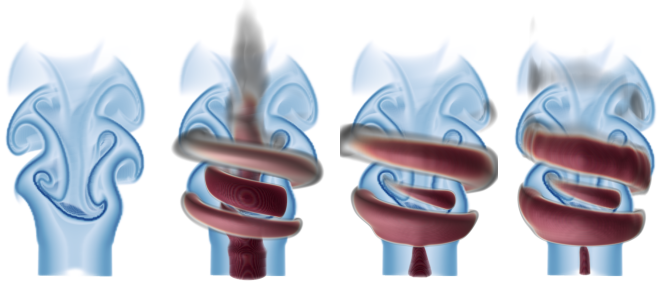

(a) FTLE (b) Galilean inv. λ_2 (c) Objective λ_2 (d) Affine inv. λ_2

Fig. 15: Vortices in a SWIRLING JET. (a) shows an FTLE field, which provides a first impression of the helical vortex structures. (b)-(d) depict λ_2 in different reference frames. Here, with $U = 41^2$.

7.6.1 Physical Interpretation

For a physical interpretation of affine invariance, imagine a vortex in a pipe, moving along the boundary for a fixed observer. Near the boundary, the flow is slower, creating shear that stretches the vortex. Nevertheless, the vortex flows forward, but its particles move at different speed. This forward motion is added to the observed velocity field and it is this difference that is removed, when transforming into the steady reference frame. Any overshadowing, whether it is by a translation, a rotation or shear, will hide the structures that can be made visible in the steady frame. Another way to look at shear is to consider it as a spatially-varying translation. Galilean invariance and objectivity assume spatially-constant translations. To remove spatially-varying motions, we consider the even more general class of affine transformations.

7.6.2 Consistency with Steady Case

A plausibility check for any technique that operates on unsteady flows is to consider what happens when vector field $\mathbf{v}$ is steady, i.e., $\mathbf{v}_t = \mathbf{0}$. In this case, none of the optimization-based methods will change the reference frame, since with $\mathbf{v}_t = \mathbf{0}$ in Eq. (18) we have $\widehat{\mathbf{y}} = \mathbf{0}$ in Eq. (17). The optimal $\overline{\mathbf{u}}$ that solves Eq. (17) is thus $\overline{\mathbf{u}} = \mathbf{0}$, and hence the transformed vector field in Eqs. (19) becomes $\overline{\mathbf{v}} = \mathbf{v}$, which holds for the all optimization-based invariance types.

7.6.3 Turbulent Flows

A characteristic property of turbulent flows is the presence of differently sized vortices, due to the large scale to small scale energy cascades [7]. Since our method fits optimal reference frames

to a local and constant neighborhood, the reference frame cannot perfectly adapt to small scale details, which is measurable by the non-vanishing residuals. Fitting to a neighborhood has a smoothing effect, which on the other hand provides robustness to noise.

7.6.4 Existence of Unique Solution

As in [10], a unique solution cannot be found if there are symmetric solutions, e.g., if the flow is rotationally-symmetric. For objectivity and similarity invariance, linear vector fields do not provide enough information to produce a full rank system in Eq. (17), no matter how large neighborhood U. Affine invariance has more degrees of freedom and does not have a unique solution for linear and quadratic vector fields. Other techniques such as FTLE are similarly not applicable in "too simple" vector fields. In real-world flows, we did not encounter such cases.

7.6.5 Interpretation of Ambient Flow

If vortices perform equal-speed translations (as it is almost the case in a von-Kármán vortex street), then the ambient flow $\widetilde{\mathbf{v}}$ in Eq. (38) is constant. If vortices, on the other hand, move on circular paths, then $\widetilde{\mathbf{v}}$ contains a perfect center flow, which then corresponds to the rotation-invariant feature flow field [11]. For (hyper-)objective methods no such a-priori knowledge about the shape of the ambient field's streamlines is available. However, vortices move coherently and thus all points inside a vortex should be observable in nearly the same steady reference frame. Thus, the ambient flow $\widetilde{\mathbf{v}}$ should be smooth within a coherent vortex. By visualizing $\widetilde{\mathbf{v}}$, the smoothness can be observed, as shown in Fig. 2 for the BOUSSINESQ flow.

7.6.6 Artificial Vortices

Individual time slices may contain artificial vortices only if the vector field is viewed in a reference frame, in which the flow is still unsteady. To extract the correct vortices, we transform the flow into an as-steady-as-possible reference frame. The advantage of our method is that the risk of artificial vortices can always be quantified by the residual. Using the new hyper-objective methods, the residual was always reduced and the result thus improved.

7.6.7 Incompressibility in Optimal Frames

The observation in a hyper-objective reference frame does not preserve the divergence, which is necessary to account for the scaling of vortices. Vortices are growing by gradually propelling more and more fluid material into a rotating motion. As an example, consider the 2D cylinder in Section 7.2.1. Each vortex feeds from the fluid that flows around the cylinder, until the vortex is large enough to detach and get carried away. In unsteady flows vortices grow. In steady flows, however, they do not. Since we view unsteady flows in a steady reference frame, the growth must be accounted for, making the observation necessarily not divergence-free.

7.6.8 Extension to Higher-Order Methods

We experimented with first-order vortex coreline extractors. Higher-order extractors [33] could be applied as well, since all spatial derivatives of $\mathbf{v}$ become reference frame invariant in the optimal frames. This would open the path to bent corelines that move on arbitrary paths, which constitutes another class of vortices that has previously been inaccessible.

7.6.9 Extension to Objective Lagrangian Vortex Measures

As in [10], frame invariant region-based counterparts to λ_2 and vorticity can be calculated in our optimal reference frames. Integrating these measures along pathlines of the original field $\mathbf{v}$ leads to Lagrangian frame invariant vortex measures. Lagrangian measures are a tool to investigate the coherence of a vortex over time, which recently gained more attention in the literature [16].

8 CONCLUSIONS

When observing fluids and the features therein, the way the observer moves should not have an impact on the result. Recently, Günther et al. [10] proposed a technique that transforms an observer into a distinguished reference frame in which the flow appears as steady as possible. In this frame, feature extraction becomes independent of the original reference frame, which ultimately allowed for an *objective* observation of many standard vortex extraction techniques. In this paper, we developed a deeper theoretical understanding of the varying degrees of freedoms that might be considered, when searching for a distinguished reference frame. Starting from general affine transformations, we gradually decreased the degrees of freedom, leading us to similarity transformations (rotation, translation and uniform scale), and objectivity, which are included as a special case. Finally, we have shown for Galilean transformations that the optimal frame is found by subtraction of the feature flow field, which sheds new light on the properties of previous techniques [47]. We have shown that the optimal reference frame transformation has lower residuals (performs better) if more degrees of freedoms are added, i.e., affine invariance generally performed best. The extraction time and the condition number increase, however, making affine invariance numerically less stable, which is due to the higher number of unknowns (degrees of freedom). We showed extraction results for various neighborhood shapes and sizes and studied the effect of the neighborhood size on the condition number and on the residuals. The smaller the neighborhood size, the smaller is the residual, but also the more the reference frame fits to noise. Thus, the neighborhood should be big enough to smooth out noise and to have sufficient numerical stability. Increasing the neighborhood size spatially smoothes the obtained reference frame. Inside a vortex, points move coherently and are thus observed in a similar reference frame. Coherence of the reference frame is the key to selecting a suitable neighborhood size. The neighborhood size may be smaller or bigger than the expected size of vortices, as long as the particles inside the neighborhood region move coherently. In the future, we would like to explore other regularizers for our energy, and apply other feature extraction techniques in the optimal reference frame.

APPENDIX A
AFFINE TRANSFORMATION OF A VECTOR FIELD

Consider an affine transformation:

$$\mathbf{x}^* = \mathbf{R}(t)\,\mathbf{x} + \mathbf{c}(t) \quad , \quad t^* = t - a \tag{44}$$

where $\mathbf{R}(t)$ is a general invertible matrix, $\mathbf{c}(t)$ is a translation vector and a is a constant. For brevity we denote $\mathbf{R}(t)$ as $\mathbf{R}$. Applying Eq. (44) transforms a vector field into a new frame:

$$\mathbf{v}^* = \mathbf{R}\,(\mathbf{v} + \mathbf{H}_1\,\mathbf{x} + \mathbf{k}_1) \tag{45}$$

$$\mathbf{J}^* = \mathbf{R}\,(\mathbf{J} + \mathbf{H}_1)\,\mathbf{R}^{-1} \tag{46}$$

$$\mathbf{a}^* = \mathbf{R}\,(\mathbf{a} + 2\,\mathbf{H}_1\,\mathbf{v} + \mathbf{H}_2\,\mathbf{x} + \mathbf{k}_2) \tag{47}$$

$$\mathbf{v}_t^* = \mathbf{R}\,(\mathbf{v}_t - \mathbf{J}\,\mathbf{H}_1\,\mathbf{x} + \mathbf{H}_1\,\mathbf{v} - \mathbf{J}\,\mathbf{k}_1 + \mathbf{H}_3\,\mathbf{x} + \mathbf{k}_3) \tag{48}$$

with

$$\mathbf{H}_1 = \mathbf{R}^{-1}\,\dot{\mathbf{R}}\,, \quad \mathbf{H}_2 = \mathbf{R}^{-1}\,\ddot{\mathbf{R}}\,, \quad \mathbf{H}_3 = \mathbf{H}_2 - \mathbf{H}_1{}^2, \quad (49)$$

$$\mathbf{k}_1 = \mathbf{R}^{-1}\,\dot{\mathbf{c}}\,, \quad \mathbf{k}_2 = \mathbf{R}^{-1}\,\ddot{\mathbf{c}}\,, \quad \mathbf{k}_3 = \mathbf{k}_2 - \mathbf{H}_1\,\mathbf{k}_1 \quad (50)$$

where $\dot{\mathbf{R}} = \frac{d\mathbf{R}}{dt}$, $\ddot{\mathbf{R}} = \frac{d\dot{\mathbf{R}}}{dt}$, $\dot{\mathbf{c}} = \frac{d\mathbf{c}}{dt}$, $\ddot{\mathbf{c}} = \frac{d\dot{\mathbf{c}}}{dt}$. The proof of Eqs. (45)–(48) is analogue to the proof of objectivity in [10].

APPENDIX B
PROOF OF AFFINE INVARIANCE

This proof follows [10], where objectivity was proven. Let $\mathbf{w}$ be the observation of $\mathbf{v}$ under an arbitrary frame $(\mathbf{P}, \mathbf{d})$, where $\mathbf{P}$ is a general invertible matrix and $\mathbf{d}$ is a translation vector.

Further, let $\overline{\mathbf{w}}$ be the observation of $\mathbf{w}$ under its optimal frame $(\mathbf{R}, \mathbf{c})$. To show the affine invariance of $\overline{\mathbf{v}}$, we follow Definition 1 and show that the optimal frames of $\mathbf{v}$ and $\mathbf{w}$ are related by:

$$\overline{\mathbf{w}} = \mathbf{P}\,\overline{\mathbf{v}} \quad (51)$$

To find $\overline{\mathbf{w}}$, we search for its optimal frame $(\mathbf{R}, \mathbf{c})$ that minimizes

$$\int_{\mathbf{P}U+\mathbf{d}} \|\mathbf{w}_t^*\|^2 dV \to \min\,. \quad (52)$$

From the perspective of $\mathbf{v}$, the optimal frame of $\mathbf{w}$ is reached by the transformation: $\mathbf{x}^* = \mathbf{R}\,(\mathbf{P}\,\mathbf{x} + \mathbf{d}) + \mathbf{c}$. Thus, $\mathbf{w}_t^*$ can be expressed from the perspective of $\mathbf{v}$, which allows us to use $\mathbf{v}_t$:

$$\mathbf{w}_t^* = \underline{\mathbf{R}}\,(\mathbf{v}_t - \mathbf{M}\,\underline{\mathbf{u}}) \quad (53)$$

where $\mathbf{x}^* = \underline{\mathbf{R}}\,\mathbf{x} + \underline{\mathbf{c}}$ with $\underline{\mathbf{R}} = \mathbf{R}\,\mathbf{P}$, $\underline{\mathbf{c}} = \mathbf{R}\,\mathbf{d} + \mathbf{c}$, and

$$\underline{\mathbf{u}} = \begin{pmatrix} -vec(\underline{\mathbf{H}}_1) \\ \underline{\mathbf{k}}_1 \\ -\underline{\mathbf{k}}_3 \\ -vec(\underline{\mathbf{H}}_3) \end{pmatrix}. \quad (54)$$

Since $\underline{\mathbf{R}}$ and $\mathbf{R}$ are affine transformations, they preserve collinearity. Thus, the temporal derivatives $\mathbf{w}_t^*$ and $\mathbf{v}_t^*$ in Eqs. (13) and (53) have the same minimizer, i.e., $\underline{\bar{\mathbf{u}}}$ minimizing (52) and $\bar{\mathbf{u}}$ minimizing (12) are identical. Given the parameters $\bar{\mathbf{u}} = \underline{\bar{\mathbf{u}}}$, we compute $\overline{\mathbf{v}}$ and $\overline{\mathbf{w}}$ in the optimal reference frame:

$$\overline{\mathbf{v}} \;=\; \mathbf{R}\,(\mathbf{v} + \overline{\mathbf{H}}_1\,\mathbf{x} + \overline{\mathbf{k}}_1) \quad (55)$$

$$\overline{\mathbf{w}} \;=\; \underline{\mathbf{R}}\,(\mathbf{v} + \bar{\underline{\mathbf{H}}}_1\,\mathbf{x} + \bar{\underline{\mathbf{k}}}_1) \quad (56)$$

and from this we get for $\mathbf{R} = \mathbf{I}$ that $\overline{\mathbf{w}} = \mathbf{P}\,\overline{\mathbf{v}}$, i.e., Eq. (51). The affine invariance of $\overline{\mathbf{J}}, \overline{\mathbf{v}}_t, \bar{\mathbf{a}}$ is shown in a similar way.

APPENDIX C
SIMILARITY INVARIANCE

We derive matrix $\mathbf{M}$ for similarity transformations (rotation, translation and uniform scale). We consider transformations:

$$\mathbf{x}^* = s(t)\;\mathbf{Q}(t)\;\mathbf{x} + \mathbf{c}(t) \quad , \quad t^* = t - a \quad (57)$$

cf. Eq. (23). For brevity we denote $\mathbf{Q}(t)$ as $\mathbf{Q}$. Applying this transformation gives the vector field and its differential properties in the new reference frame:

$$\mathbf{v}^* = s\,\mathbf{Q}\;(\mathbf{v} + \mathbf{H}_1\,\mathbf{x} + \mathbf{k}_1) \quad (58)$$

$$\mathbf{J}^* = \mathbf{Q}\;(\mathbf{J} + \mathbf{H}_1)\;\mathbf{Q}^{\mathrm{T}} \quad (59)$$

$$\mathbf{a}^* = s\,\mathbf{Q}\;(\mathbf{a} + 2\,\mathbf{H}_1\,\mathbf{v} + \mathbf{H}_2\,\mathbf{x} + \mathbf{k}_2) \quad (60)$$

$$\mathbf{v}_t^* = s\,\mathbf{Q}\;(\mathbf{v}_t - \mathbf{J}\,\mathbf{H}_1\,\mathbf{x} + \mathbf{H}_1\,\mathbf{v} - \mathbf{J}\,\mathbf{k}_1 + \mathbf{H}_3\,\mathbf{x} + \mathbf{k}_3) \quad (61)$$

with

$$\mathbf{H}_1 = \mathbf{Q}^{\mathrm{T}}\,\dot{\mathbf{Q}} + \frac{\dot{s}}{s}\,\mathbf{I} \quad (62)$$

$$\mathbf{H}_2 = \mathbf{Q}^{\mathrm{T}}\,\ddot{\mathbf{Q}} + 2\,\frac{\dot{s}}{s}\,\mathbf{Q}^{\mathrm{T}}\,\dot{\mathbf{Q}} + \frac{\ddot{s}}{s}\,\mathbf{I} \quad (63)$$

$$\mathbf{H}_3 = \mathbf{H}_2 - \mathbf{H}_1{}^2 \quad (64)$$

$$\mathbf{k}_1 = \frac{1}{s}\,\mathbf{Q}^{\mathrm{T}}\,\dot{\mathbf{c}}\,, \quad \mathbf{k}_2 = \frac{1}{s}\,\mathbf{Q}^{\mathrm{T}}\,\ddot{\mathbf{c}}\,, \quad \mathbf{k}_3 = \mathbf{k}_2 - \mathbf{H}_1\,\mathbf{k}_1 \quad (65)$$

where $\dot{\mathbf{Q}} = \frac{d\mathbf{Q}}{dt}$, $\ddot{\mathbf{Q}} = \frac{d\dot{\mathbf{Q}}}{dt}$, $\dot{\mathbf{c}} = \frac{d\mathbf{c}}{dt}$, $\ddot{\mathbf{c}} = \frac{d\dot{\mathbf{c}}}{dt}$, $\dot{s} = \frac{ds}{dt}$, $\ddot{s} = \frac{d\dot{s}}{dt}$ are the time derivatives of $\mathbf{Q}$, s, and $\mathbf{c}$. The proof of Eqs. (58)–(61) is analogue to the proof for objectivity in [10]. We rewrite Eq. (61):

$$\mathbf{v}_t^* = \mathbf{Q}\;(\mathbf{v}_t - \mathbf{M}\,\mathbf{u}) \quad (66)$$

with the 3×14 matrix $\mathbf{M}$ in 3D

$$\mathbf{M} = (-\mathbf{J}\,\mathbf{X} + \mathbf{V}\;,\;\mathbf{J}\;,\;\mathbf{X}\;,\;\mathbf{I}\;,\;-\mathbf{J}\,\mathbf{x} + \mathbf{v}\;,\;\mathbf{x}) \quad (67)$$

with $\mathbf{X} = sk(\mathbf{x})$ and $\mathbf{V} = sk(\mathbf{v})$, and the 14-vector $\mathbf{u}$

$$\mathbf{u} = \begin{pmatrix} \mathbf{u}_1 \\ \mathbf{u}_2 \\ \mathbf{u}_3 \\ \mathbf{u}_4 \\ u_5 \\ u_6 \end{pmatrix} = \begin{pmatrix} ap(\mathbf{Q}^{\mathrm{T}}\dot{\mathbf{Q}}) \\ \mathbf{k}_1 \\ ap(\mathbf{Q}^{\mathrm{T}}\ddot{\mathbf{Q}} - (\mathbf{Q}^{\mathrm{T}}\dot{\mathbf{Q}})^2) \\ -\mathbf{k}_3 \\ -\frac{\dot{s}}{s} \\ -\frac{s\,\ddot{s} - \dot{s}^2}{s^2} \end{pmatrix}. \quad (68)$$

In 2D, $\mathbf{M}$ is a 2×8 matrix

$$\mathbf{M} = (-\mathbf{J}\,\mathbf{x}_p + \mathbf{v}_p\;,\;\mathbf{J}\;,\;\mathbf{x}_p\;,\;\mathbf{I}\;,\;-\mathbf{J}\,\mathbf{x} + \mathbf{v}\;,\;\mathbf{x}) \quad (69)$$

with $\mathbf{x}_p = (-y, x)^{\mathrm{T}}$, $\mathbf{v}_p = (-v, u)^{\mathrm{T}}$, and $\mathbf{u}$ is an 8-vector. Similar to [10], we search for $\dot{\mathbf{Q}}$, $\ddot{\mathbf{Q}}$, $\dot{s}$, $\ddot{s}$, $\dot{\mathbf{c}}$, $\ddot{\mathbf{c}}$ to minimize the magnitude of the temporal derivative

$$\int_U \|\mathbf{v}_t^*\|^2 dV \to \min \quad (70)$$

within a local neighborhood by using Eqs. (17) and (18). Let $\overline{\mathbf{u}} = (\overline{\mathbf{u}}_1, \overline{\mathbf{u}}_2, \overline{\mathbf{u}}_3, \overline{\mathbf{u}}_4, \overline{u_5}, \overline{u_6})^{\mathrm{T}}$ be such an optimal $\mathbf{u}$. Then, the new fields in the locally optimal reference frame are

$$\overline{\mathbf{v}} = \mathbf{v} + sk(\overline{\mathbf{u}}_1)\,\mathbf{x} - \overline{u_5}\,\mathbf{x} + \overline{\mathbf{u}}_2 \quad (71)$$

$$\overline{\mathbf{J}} = \mathbf{J} + sk(\overline{\mathbf{u}}_1) - \overline{u_5}\,\mathbf{I} \quad (72)$$

which follows from insertion of $\overline{\mathbf{u}}_1, \overline{\mathbf{u}}_2, \overline{u_5}$ into Eqs. (58)–(59).

ACKNOWLEDGMENTS

The 2D CYLINDER data set and the BOUSSINESQ flow were simulated with Gerris Flow solver [30]. The resampled version of the latter was kindly provided by Tino Weinkauf. The CENTRIFUGAL PUMP is courtesy of the Institute of Applied Mechanics, Clausthal University, Germany and was made available by Andreas Lucius for the IEEE Visualization Contest 2011. We thank Vinicius C. Azevedo for providing the cut-cell solver [2], used for the MOVING OBSTACLE flow. The resampled version of the SQUARE CYLINDER flow was provided by Tino Weinkauf and the simulation was computed by Camarri et al. [6]. The SWIRLING JET simulation was provided by Moritz Sieber from TU Berlin, Germany, who we would also like to thank for the discussions on the jet flow. All visualizations were rendered with the visualization tool Amira [40].

REFERENCES

[1] G. Astarita. Objective and generally applicable criteria for flow classification. *Journal of Non-Newtonian Fluid Mechanics*, 6(1):69–76, 1979.

[2] V. C. Azevedo, C. Batty, and M. M. Oliveira. Preserving geometry and topology for fluid flows with thin obstacles and narrow gaps. *ACM Trans. Graph.*, 35(4):97:1–97:12, July 2016. doi: 10.1145/2897824.2925919

[3] H. Bhatia, G. Norgard, V. Pascucci, and P.-T. Bremer. The Helmholtz-Hodge decomposition–A survey. *IEEE Transactions on Visualization and Computer Graphics*, 19(8):1386–1404, 2013.

[4] H. Bhatia, V. Pascucci, R. M. Kirby, and P.-T. Bremer. Extracting features from time-dependent vector fields using internal reference frames. *Computer Graphics Forum (Proc. EuroVis)*, 33(3):21–30, 2014.

[5] R. Bujack, M. Hlawitschka, and K. I. Joy. Topology-inspired Galilean invariant vector field analysis. In *IEEE Pacific Visualization Symposium*, pp. 72–79, April 2016. doi: 10.1109/PACIFICVIS.2016.7465253

[6] S. Camarri, M.-V. Salvetti, M. Buffoni, and A. Iollo. Simulation of the three-dimensional flow around a square cylinder between parallel walls at moderate Reynolds numbers. In *XVII Congresso di Meccanica Teorica ed Applicata*, 2005.

[7] A. J. Chorin. *Vorticity and turbulence*, vol. 103. Springer Science & Business Media, 2013.

[8] R. Drouot and M. Lucius. Approximation du second ordre de la loi de comportement des fluides simples. lois classiques déduites de lintroduction dun nouveau tenseur objectif. *Archiwum Mechaniki Stosowanej*, 28(2):189–198, 1976.

[9] T. Günther. *Opacity Optimization and Inertial Particles in Flow Visualization*. PhD thesis, University of Magdeburg, June 2016.

[10] T. Günther, M. Gross, and H. Theisel. Generic objective vortices for flow visualization. *ACM Transactions on Graphics (Proc. SIGGRAPH)*, 36(4):141:1–141:11, 2017.

[11] T. Günther, M. Schulze, and H. Theisel. Rotation invariant vortices for flow visualization. *IEEE Transactions on Visualization and Computer Graphics (Proc. IEEE SciVis 2015)*, 22(1):817–826, 2016.

[12] T. Günther and H. Theisel. Vortex cores of inertial particles. *IEEE Trans. on Vis. and Comp. Graph. (Proc. IEEE SciVis)*, 20(12):2535–2544, 2014.

[13] T. Günther and H. Theisel. The state of the art in vortex extraction. *Computer Graphics Forum*, 37(6):149–173, 2018.

[14] G. Haller. An objective definition of a vortex. *Journal of Fluid Mechanics*, 525:1–26, 2005.

[15] G. Haller. Lagrangian coherent structures. *Annual Review of Fluid Mechanics*, 47:137–162, 2015.

[16] G. Haller, A. Hadjighasem, M. Farazmand, and F. Huhn. Defining coherent vortices objectively from the vorticity. *Journal of Fluid Mechanics*, 795:136–173, 2016.

[17] J. C. R. Hunt. Vorticity and vortex dynamics in complex turbulent flows. *Transactions on Canadian Society for Mechanical Engineering (Proc. CANCAM)*, 11(1):21–35, 1987.

[18] J. Jeong and F. Hussain. On the identification of a vortex. *Journal of Fluid Mechanics*, 285:69–94, 1995.

[19] J. Kasten, I. Hotz, B. R. Noack, and H.-C. Hege. On the extraction of long-living features in unsteady fluid flows. In *Topological Methods in Data Analysis and Visualization*, pp. 115 – 126. 2011.

[20] J. Kasten, J. Reininghaus, I. Hotz, and H.-C. Hege. Two-dimensional time-dependent vortex regions based on the acceleration magnitude. *IEEE Trans. on Vis. and Comp. Graph. (SciVis)*, 17(12):2080–2087, 2011.

[21] J. Kasten, J. Reininghaus, H. I., H.-C. Hege, B. R. Noack, G. Daviller, and M. Morzynski. Acceleration feature points of unsteady shear flows. *Archives of Mechanics*, 68(1):to appear, 2016.

[22] A. Kuhn, C. Rössl, T. Weinkauf, and H. Theisel. A benchmark for evaluating FTLE computations. In *Proc. IEEE Pacific Visualization Symposium (PacificVis 2012)*, pp. 121–128. Songdo, Korea, 2012.

[23] R. Laramee, H. Hauser, L. Zhao, and F. Post. Topology-based flow visualization, the state of the art. In *Topology-based Methods in Visualization*, pp. 1–19. Springer Berlin Heidelberg, 2007.

[24] H. J. Lugt. The dilemma of defining a vortex. In *Recent developments in theoretical and experimental fluid mechanics*, pp. 309–321. 1979.

[25] R. S. Martins, A. S. Pereira, G. Mompean, L. Thais, and R. L. Thompson. An objective perspective for classic flow classification criteria. *Comptes Rendus Mecanique*, 344:52–59, 2016. doi: 10.1016/j.crme.2015.08.002

[26] A. Okubo. Horizontal dispersion of floatable particles in the vicinity of velocity singularities such as convergences. *Deep Sea Research and Oceanographic Abstracts*, 17(3):445–454, 1970.

[27] T. Peacock, G. Froyland, and G. Haller. Introduction to focus issue: Objective detection of coherent structures. *Chaos*, 25(8):087201, 2015.

[28] R. Peikert and M. Roth. The "parallel vectors" operator – a vector field visualization primitive. In *Proc. IEEE Visualization*, pp. 263–270, 1999.

[29] A. E. Perry and M. S. Chong. Topology of flow patterns in vortex motions and turbulence. *Applied Scientific Research*, 53(3):357–374, 1994.

[30] S. Popinet. Free computational fluid dynamics. *Cluster World 2*, (6), 2004.

[31] F. H. Post, B. Vrolijk, H. Hauser, R. S. Laramee, and H. Doleisch. The state of the art in flow visualisation: Feature extraction and tracking. *Computer Graphics Forum*, 22(4):775–792, 2003.

[32] S. K. Robinson. Coherent motions in the turbulent boundary layer. *Annual Review of Fluid Mechanics*, 23(1):601–639, 1991.

[33] M. Roth and R. Peikert. A higher-order method for finding vortex core lines. In *Proc. IEEE Visualization*, pp. 143–150, 1998.

[34] J. Sahner, T. Weinkauf, and H.-C. Hege. Galilean invariant extraction and iconic representation of vortex core lines. In *Proc. Eurographics / IEEE VGTC Symposium on Visualization (EuroVis)*, pp. 151–160, 2005.

[35] J. Sahner, T. Weinkauf, N. Teuber, and H.-C. Hege. Vortex and strain skeletons in Eulerian and Lagrangian frames. *IEEE Transactions on Visualization and Computer Graphics*, 13(5):980–990, 2007.

[36] T. Schafhitzel, J. Vollrath, J. Gois, D. Weiskopf, A. Castelo, and T. Ertl. Topology-preserving λ_2-based vortex core line detection for flow visualization. *Computer Graphics Forum*, 27(3):1023–1030, 2008.

[37] W. J. Schroeder, B. Lorensen, and K. Martin. *The visualization toolkit: an object-oriented approach to 3D graphics*. Kitware, 2004.

[38] M. Serra and G. Haller. Forecasting long-lived lagrangian vortices from their objective eulerian footprints. *J. Fluid Mech.*, p. to appear, 2016.

[39] M. Serra and G. Haller. Objective eulerian coherent structures. *Chaos: An Interdisciplinary Journal of Nonlinear Science*, 26(5):053110, 2016.

[40] D. Stalling, M. Westerhoff, and H.-C. Hege. Amira: A highly interactive system for visual data analysis. In *The Visualization Handbook*, pp. 749–767. Elsevier, 2005.

[41] D. Sujudi and R. Haimes. Identification of swirling flow in 3D vector fields. Technical report, Departement of Aeronautics and Astronautics, MIT, 1995. AIAA Paper 95-1715.

[42] M. Tabor and I. Klapper. Stretching and alignment in chaotic and turbulent flows. *Chaos, Solitons & Fractals*, 4(6):1031–1055, 1994.

[43] H. Theisel and H.-P. Seidel. Feature flow fields. In *Proc. Symposium on Data Visualisation*, pp. 141–148, 2003.

[44] R. L. Thompson. Some perspectives on the dynamic history of a material element. *Int. Journal of Engineering Science*, 46(3):224–249, 2008.

[45] Y. Tong, S. Lombeyda, A. N. Hirani, and M. Desbrun. Discrete multiscale vector field decomposition. *ACM Trans. Graph. (Proc. SIGGRAPH)*, 22(3):445–452, 2003.

[46] C. Truesdell and W. Noll. *The nonlinear field theories of mechanics*. Handbuch der Physik, Band III/3, Springer-Verlag, Berlin, 1965.

[47] T. Weinkauf, J. Sahner, H. Theisel, and H.-C. Hege. Cores of swirling particle motion in unsteady flows. *IEEE Transactions on Visualization and Computer Graphics (Proc. Visualization)*, 13(6):1759–1766, 2007.

[48] J. Weiss. The dynamics of enstrophy transfer in two-dimensional hydrodynamics. *Physica D: Nonlin. Phenomena*, 48(2-3):273–294, 1991.

[49] A. Wiebel. Feature detection in vector fields using the Helmholtz-Hodge decomposition. Diploma thesis, Univ. Kaiserslautern, 2004.

Tobias Günther joined the Computer Graphics Laboratory (CGL) at the ETH Zürich as a postdoctoral researcher in 2016. He received his M.Sc. in Computer Science in 2013 and his Dr.-Ing. (Ph.D.) in 2016 both from the Otto-von-Guericke University of Magdeburg. His research interests include scientific visualization, progressive light transport and real-time rendering.

Holger Theisel is professor for Visual Computing at the Computer Science Department at University of Magdeburg, Germany. In 1994, he received the diploma in Computer Science, in 1996 a Ph.D. in Computer Science, and a habilitation (venia legendi) in 2001 from the University of Rostock. His research interests focus on flow visualization as well as on CAGD, geometry processing and information visualization.